J. Fluid Mech. (2008), *vol.* 602, *pp.* 327–382. © 2008 Cambridge University Press
doi:10.1017/S0022112008000803 Printed in the United Kingdom

Vortical structures in the turbulent boundary layer: a possible route to a universal representation

MICHEL STANISLAS, LAURENT PERRET† AND JEAN-MARC FOUCAUT

Ecole Centrale de Lille, Laboratoire de Mécanique de Lille, Boulevard Paul Langevin, 59655 Villeneuve d'Ascq, France

(Received 14 May 2007 and in revised form 23 January 2008)

A study of streamwise oriented vortical structures embedded in turbulent boundary layers is performed by investigating an experimental database acquired by stereoscopic particle image velocimetry (SPIV) in a plane normal both to the mean flow and the wall. The characteristics of the experimental data allow us to focus on the spatial organization within the logarithmic region for Reynolds numbers Re_θ up to 15 000. On the basis of the now accepted hairpin model, relationships and interaction between streamwise vortices are first investigated via computation of two-point spatial correlations and the use of linear stochastic estimation (LSE). These analyses confirm that the shape of the most probable coherent structures corresponds to an asymmetric one-legged hairpin vortex. Moreover, two regions of different dynamics can be distinguished: the near-wall region below $y^+ = 150$, densely populated with strongly interacting vortices; and the region above $y^+ = 150$ where interactions between eddies happen less frequently. Characteristics of the detected eddies, such as probability density functions of their radius and intensity, are then studied. It appears that Reynolds number as well as wall-normal independences of these quantities are achieved when scaling with the local Kolmogorov scales. The most probable size of the detected vortices is found to be about 10 times the Kolmogorov length scale. These results lead us to revisit the equation for the mean square vorticity fluctuations, and to propose a new balance of this equation in the near-wall region. This analysis and the above results allow us to propose a new description of the near-wall region, leading to a new scaling which seems to have a good universality in the Reynolds-number range investigated. The possibility of reaching a universal scaling at high enough Reynolds number, based on the external velocity and the Kolmogorov length scale is suggested.

1. Introduction

Despite their apparent random character, wall-bounded turbulent flows are now known to consist of well-organized turbulent structures which play a key role in generating and sustaining turbulence. A large amount of work has been devoted to the study of these coherent structures over the last five decades and, though their

† Present address: Ecole Centrale de Nantes, Laboratoire de Mécanique des Fluides, 1 rue de la Noe, 44321 Nantes, France.

creation process and their dynamics are still not fully understood, general agreement has been reached concerning their nature: streamwise vortices, low- and high-speed velocity regions (streaks), sweeps and ejections, and hairpin- or cane-shaped vortices constitute the main coherent structures near the wall. Robinson (1991) and Panton (1997) provide extensive overviews on the investigation of wall turbulence coherent structures. Adrian (2007) has provided an extensive synthesis of the knowledge about vortical structures in wall turbulence.

The model of hairpin-shaped (or horseshoe) vortices was first proposed by Theodorsen (1952) to explain many features of wall turbulence and was later confirmed experimentally, by flow visualization by Head & Bandyopadhyay (1981). This idealized vortical structure is characterized by its three-dimensional structure, which consists of a pair of counter-rotating legs and a head segment joined by two necks to the legs. The work of Head & Bandyopadhyay (1981) has motivated many studies to investigate and confirm the nature and the role of hairpin-like structures (Robinson 1991). It should be noted that several studies reported asymmetric hairpins or 'cane' vortices rather than symmetric ones (Choi & Guezennec 1989; Guezennec, Piomelli & Kim 1989; Robinson 1991). Since the early contribution by Spalart (1989), direct numerical simulation (DNS) of turbulent flows has offered the possibility of studying both in space and time, the birth and the development of coherent structures (Robinson 1991; Brooke & Hanratty 1993; Panton 1997; Zhou *et al.* 1999). For a long time, the main problem of DNS was the range of Reynolds numbers reached, which did not allow the development of a real log region, either in channels, or in boundary layers. The progress of supercomputers has recently allowed DNS of channel flows to reach Reynolds numbers which can be considered as relevant and free from low-Reynolds-number effects.

Tanahashi *et al.* (2004), Kang, Tanahashi & Miyauchi (2005) and Das *et al.* (2006) performed an extensive study of fine-scale eddies in channel flows at Reynolds number $Re_\tau = hu_\tau/\nu = h^+$ (where h is half the channel height) from 100 to 1270. They developed a specific detection algorithm, based on the second invariant Q of the velocity gradient tensor and requesting no threshold. They identified 'coherent' fine eddies' which appear in the whole wall layer (from $y^+ = 1$ to the channel centreline) and which scale with Kolmogorov micro-scales when varying the Reynolds number. The most intense eddies have a size of 10 to 12 η (the whole range being between 6 and 90 η) and their intensity scales with $u_{rms} = \sqrt{u_i' u_i'/3}$ (while the whole range of vortices observed scales better on the Kolmogorov velocity scale). Away from the wall, they look much like the fine eddies found in isotropic turbulence. Near the wall, they are stronger (up to $3u_{rms}$) and subject to large compression and stretching. It is interesting that the authors could fit a model to the vortices. By determining the direction of the vorticity vector in the vortices and by projecting the velocity field in a plane normal to this vector, they show that the velocity distribution around the vortex centre is well fitted by a Burger's vortex. The maximum tangential velocity is of the order of 0.5 to 0.6 u_{rms} and the circulation scales with η and u_{rms} whatever the wall distance is. Consequently, the diameter and tangential velocity of the eddies are correlated.

Beside this work performed in Japan, which is part of a broader study of fine-scale eddies in turbulence (Tanahashi *et al.* 1997, 2001), there has been a joint effort for several years by Stanford, Urbana Champaign and Madrid Universities to perform and analyse high-Reynolds-number DNS of channel flow (Jimenez *et al.* 2004; del Álamo *et al.* 2006; del Álamo & Jimenez 2006). The most recent paper of this group summarizes their main results and understanding of the vortical organization in the

logarithmic layer. From the analysis of five different DNS with a range of Re_τ from 180 to 1900, they were able to assess the main characteristics of the vortical structures present in the wall layer. To identify the vortices, they use the discriminant criterion of Chong, Perry & Cantwell (1990), but with a variable threshold based on the local value of the standard deviation of this discriminant. This allows them to extract a volume fraction of vortices that does not depend on Reynolds number. Vortices are defined as connected sets of points satisfying the above criterion, and spanwise vortices are those having their vorticity vector forming an angle of less than 30° to the spanwise direction. These spanwise vortices are characterized by fitting an elliptical Gaussian vortex on an (x, y) cut (streamwise/wall-normal plane). Scaling the results with η and u_{rms} shows Reynolds-number invariance and good agreement with a previous study by the same group, using the same vortex model for isotropic turbulence (Jimenez & Wray 1998). In contrast, the agreement with Tanahashi *et al.* (2004) is not so good. The vortices are 20% thinner, which may be explained by a different definition of the diameter, but twice as strong, which is justified by the authors based on the fact that they detect only the strongest vortices with their method. Examining the distribution in space of these vortices, they identify two types of vortex clusters: small individuals detached from the wall; and tall objects attached to the wall. The wall-detached clusters cover a wide spectrum of shapes having some similarity with isotropic turbulence and scaling with Kolmogorov scales. The tall attached objects are rooted around $y^+ = 20$ and show self-similarity. The average structure obtained by scaling individual ones on their height coincides with the image of a large-scale hairpin, but individuals are much more complex. Very long regions of low streamwise velocity are identified downstream of these tall clusters. The angle with the wall of these vortices varies from 12° near the wall to 90° at the top with an overall angle around 45°. New clusters seem to appear at the upstream edge of older ones and their spreading in space seems mostly linked to diffusion by background fluctuations. Finally, the estimated lifetime of these clusters appears too short for them to grow from the wall, indicating that some may be generated directly in the log layer.

As can be seen, by giving access to the full three-dimensional fields of primitive variables, promising and comprehensive results can now be extracted from DNS, bringing important insights into the structure of turbulent flows. Nevertheless, although significant progress has been achieved in the last ten years, the Reynolds number is still far from practical application in, for example, the field of aeronautics. Consequently, these numerical contributions must be complemented by experiments which are much more restricted in terms of the data they can assess, but which can be designed to reach high Reynolds numbers. Hopefully, a detailed investigation of high-Reynolds-number flows, in which the logarithmic region exists between the buffer layer and the wake region, has recently been made possible, thanks to the development of advanced experimental techniques. In particular, particle image velocimetry (PIV) has proved to be a reliable tool for performing multi–point measurements in turbulent flows (Adrian 1991; Foucaut, Carlier & Stanislas 2004), by providing two-dimensional velocity maps, the accuracy of which is now well characterized and the statistics agree well with hot-wire anemometry.

Adrian, Meinhart & Tomkins (2000*b*) were among the first to use PIV to investigate streamwise–wall normal planes in a turbulent boundary layer. They performed measurements for Reynolds number Re_θ ranging from 930 to 6845. They showed that hairpin vortices, identified by a vortex core located above the region of a strong second-quadrant event, frequently occur in the outer region of the boundary layer.

These structures were found to align coherently in the streamwise direction, forming groups of vortices consistent with the hairpin packets highlighted by Zhou *et al.* (1999) in their DNS of a channel flow. They proposed that these packets, originating from the near-wall region, grow upwards in a ramp–like arrangement inclined at an angle near 12°, inducing a low-momentum region beneath the inclined interface. They found that an important feature of the logarithmic region is the occurrence of smaller hairpin packets in the environment of larger hairpin packets. Christensen & Adrian (2001) showed statistical evidence of the presence of hairpin packets in the outer region of turbulent channel flow at Reynolds number $Re_\tau = 547$ and 1764 also from PIV measurements. They confirmed the 12° inclination angle from the wall of the upper interface of the hairpin packets. Tomkins & Adrian (2003) used PIV to investigate streamwise–spanwise planes (parallell to the wall) in the whole logarithmic layer at $Re_\theta = 1015$ and 7705. Again, consistency with the hairpin packet model was shown by the finding of streamwise elongated regions of low momentum, bordered by vortices. In this work, spanwise length scales based on statistical analysis were found to grow linearly with wall distance, suggesting that the coherent structures grow self-similarly in time (in agreement with del Álamo *et al.* 2006). On the contrary, based on the investigation of instantaneous fields, the scale growth mechanism appears to rely on the merging or coalescence of vortex packets.

Ganapathisubramani, Longmire & Marusic (2003), by performing stereoscopic PIV measurements in the same streamwise–spanwise plane, confirmed the existence of such a large-scale organization. Two experimental studies repeated the experiment of Head & Bandyopadhyay (1981), with the same inclined cross-stream light-sheet configuration, but using PIV to obtain quantitative information on coherent structures. The work of Carlier & Stanislas (2005) was focused on the eddy structures present in the boundary layer at Reynolds numbers Re_θ between 8000 and 19 000. For the range of Reynolds number investigated, the characteristics of the educed vortices were found to be universal in wall units, forming in the near-wall region and then moving away from the wall. Above the buffer layer, the circulation of these eddy structures appears nearly constant, resulting in a slow decrease of their vorticity and a slow increase of their radius. Near the wall, results corroborate existing models and support the universality of the mechanisms in this region. Hutchins, Hambleton & Marusic (2005) limited their study to Reynolds numbers Re_θ up to 7440. By investigating planes inclined at both 45° and 135° to the streamwise axis, they highlighted the existence of inclined eddies bordering low-momentum regions, with a non-negligible probability of appearing in a counter-rotating pair in the 135° plane. In the outer region, spanwise length scales appear to scale with the outer variables. The computation of the two–point correlations of the longitudinal velocity component with respect to the wall–normal distance reveals two regimes designated by the authors as 'attached' to or 'detached' from the buffer layer, which indicates that coherent structures progressively decouple from the wall as they migrate away from it (in agreement with del Álamo *et al.* 2006).

This investigation has been pursued by the same group (Ganapathisubramani *et al.* 2006) using a more sophisticated dual-plane PIV technique. This approach allowed these authors to assess both the three components of the instantaneous velocity and the full velocity gradient tensor in a plane parallel to the wall. The study was performed in a turbulent boundary layer at $Re_\theta = 2800$ and at two wall distances corresponding to the log region ($y^+ = 110$) and the outer wake region ($y/\delta = 0.53$). From these data, they could extract both the instantaneous velocity and vorticity vectors. The r.m.s. values of the vorticity agree well with the existing literature, showing that the

velocity gradients are properly assessed. To detect the coherent vortices (the legs of the hairpins), these authors used the swirling strength, which is now an accepted criterion for this purpose (Chakraborty, Balachandar & Adrian 2005), in both its three-dimensional and two-dimensional form. The analysis of the auto–correlation of the signed swirling strength λ_{3D}, coupled to a quadrant decomposition of the vorticity vector projection in the (x, y)-plane, leads these authors to propose a model of forward-leaning and backward-leaning Λ-shaped vortices. They also analyse in detail the statistics of the angle of the vorticity vector associated with the coherent vortices, with respect to the different coordinate planes. Putting aside by a proper threshold the heads and the streamwise vortices, they show that the remaining vortices have an average angle of $\pm 38^\circ$ with the wall ((x, z)-plane) at $y^+ = 110$ and $\pm 33^\circ$ at $y/\delta = 0.53$. This angle goes to $\pm 45^\circ$ when it is projected in the (x, y)-plane, which is in good agreement with the literature. They detect a majority of forward-leaning vortex filaments, especially in the log region, but also a non-negligible amount of backward-leaning vortices, which are in comparable numbers at both locations. The angle of these vortices with the (x, y)-plane (so projected in the (x, z)-plane) is of the order of $\pm 15^\circ$, showing that these structures are (on average) more or less aligned with the main stream, with a Λ shape in good agreement with the model of Perry & Marusic (1995). In a concomitant investigation, Hambleton, Hutchins & Marusic (2006) performed a PIV investigation of a turbulent boundary layer, using two orthogonal StereoPIV planes at the same time. One plane was parallel to the wall ((x, z)-plane) and the other normal to the wall and parallel to the flow ((x, y)-plane). The boundary layer was nearly the same as in the previous study ($Re_\theta = 2800$). The horizontal plane was set again in the log region ($y^+ = 98$). The spatial resolution was 16 wu (wall units) in the (x, y)-plane and 17.5 wu in the (x, z)-plane. The main interest of the study was in the use of linear stochastic estimation (LSE, see Adrian & Moin 1988) conditioned by a positive swirling strength in the vertical plane at $y/\delta = 0.19$ (that is in the upper region of the log layer). The results underline that 'the time-averaged conditional event is an inclined hairpin structure, with an inclination angle close to 45°'. Between the legs of this conditional eddy, the authors evidence a 'pronounced elongated low-speed region'. The flow pattern resulting from this analysis is in good agreement with the vortex packet model of Zhou *et al.* (1999). The same analysis performed on an event of opposite sign (retrograde vortex), shows, in the vertical plane and mostly in the outer part of the boundary layer, a pair of counter-rotating vortices also forming an angle of 45° with the wall. This second type of structure is nevertheless much less numerous than the first one.

Finally, in the same vein as the studies by Adrian and colleagues, Wu & Christensen (2006) have performed a thorough study of the Reynolds-number influence on the spanwise vortices of both the channel flow and the turbulent boundary layer. They used standard PIV in a plane normal to the wall and parallel to the flow ((x, y)-plane). They took care to keep a sufficient and nearly constant resolution in wall units (of the order of 10 wu) for the different Reynolds numbers, in order to ensure the resolution of the smallest structures. Here again, they use the signed swirling strength as a detection criterion and simply threshold this criterion to obtain the area occupied by the vortices. In agreement with Carlier & Stanislas (2005), they evidence a dense population of prograde and retrograde spanwise vortices, with the progrades largely prevailing near the wall and decreasing with y for both flows and at all Reynolds numbers. The retrograde population increases from the wall to the top of the log layer and then decreases with y for boundary layers. Scaled in outer

variables, the population density of both types of structure increases with Reynolds number. The wall variable scaling also evidences Reynolds-number influence, but opposite: the population density decreases with increasing Reynolds number in the log layer. To compare the two populations, they defined a vortex population fraction which appears universal in wall units up to the limit of the log layer and for high enough Reynolds number (Re_τ larger than about 1000). These authors also show that these vortices, together with their immediate surroundings bring a significant contribution to the mean shear, contribution which decreases with increasing Reynolds number. Finally, Wu & Christensen (2006) analysed the advection velocity of the spanwise vortices. In agreement with Carlier & Stanislas (2005), they found that the mean advection velocity is equal to the local mean flow velocity, but they evidenced a significant distribution around this mean. This distribution, which can reach 30 % of the mean near the wall, decreases progressively to 10–15 % in the wake region.

To summarize, there is a global convergence, both from DNS and experiments toward a model of hairpin packets (Zhou *et al.* 1999) attached to the wall in the lower part of the log layer and nearer to isotropic turbulence in the outer part. The agreement is also fairly good on the quantitative characteristics (size, separation, intensity, angles, etc.) of this model, but universal scaling is still unclear.

Concerning the buffer layer, because of its small size in standard facilities, very few quantitative studies are available. Lin (2006) performed an extensive study of this region. This work was done on data recorded in the same wind tunnel as in the present study and for a Reynolds number $Re_\theta = 7800$. Samples of 500 StereoPIV velocity maps were available in ten planes parallel to the wall, regularly distributed between 14 and 50 wu. Lin (2006) analysed the flow structure in detail, using spatial correlation and pattern recognition. His results confirm that the spanwise spacing of the streaks is about 120 wu and that the high-speed streaks are slightly larger than the low-speed streaks. They put in evidence streamwise vortices located between the streaks, the centre of which is located between 20 and 30 wu from the wall. An important result of this study is that, in this buffer layer, the ejections and sweeps are closely linked to the streamwise vortices. This leads to a simplification of the organization picture in this region: the important structures are the streaks (low and high) and the vortices which form between them. A paper is in preparation on this study. The thesis is in English and available from M. Stanislas.

As can be seen, much progress has been made in the last few years in the detailed description and understanding of the near-wall turbulence structure. Putting together the results from the above-mentioned DNS and experiments, a fairly complete and relatively quantitative view of the turbulence structure near the wall is provided: hairpin-like quasi-streamwise vortices organize around elongated low-speed regions with significant second quadrant events. It is clear, from this picture, that vortices play a key role in this organization, but this role is not yet fully established. The aim of the present paper is thus to investigate further the dynamics of coherent eddies present in both the buffer layer and the logarithmic region of a flat-plate boundary layer, by taking advantage of spatially well-resolved stereoscopic PIV measurements performed in a plane normal to both the flow and the wall and of some advanced mathematical tools. In particular, spanwise symmetry of the hairpin-shaped structures, scaling and relationships between the vortical structures are addressed. Consequences of these observations in terms of the scaling of the transport equation for the mean square of the fluctuating vorticity are then looked at. Finally, in the discussion, the description and scaling of the boundary layer itself are revisited.

In the present study, two relatively high Reynolds numbers, $Re_\theta = 7800$ and $Re_\theta = 15000$, for which a well-developed logarithmic region exists, are investigated with SPIV. Swirling strength correlation and linear stochastic estimation are used to analyse the flow organization linked to the vortices. A reliable criterion to extract vortices in turbulent flows has been the subject of extensive discussions. The swirling strength has been shown by Zhou *et al.* (1999) to be adequate and Chakraborty *et al.* (2005) have shown that an analytical relationship exists between the different existing criteria based on the gradient tensor, making them equivalent. Signed with the vorticity sign, the swirling strength allows one to distinguish between positive and negative rotating vortices, which is of interest in the present study. Linear stochastic estimation was first introduced by Adrian & Moin (1988) and Adrian (1993) and has been shown since then to be a useful tool for analysing the structure of various turbulent flows, including near-wall flows (Guezennec 1989). The detection of eddy structures from the PIV velocity fields used here is close to the approach of Das *et al.* (2006). It is based on the computation of the two-dimensional swirling strength from the available components of the velocity gradient tensor and on the vortex validation method proposed by Carlier & Stanislas (2005) which fits an Oseen vortex model on the detected vortices, providing quantitative characteristics of the validated vortices.

2. Experiment

The experimental set-up and the means of measurement employed in the present study are briefly described in this section. Further details on the wind tunnel, its characterization via extensive hot-wire measurements and the PIV set-up can be found in Carlier (2001) and Carlier & Stanislas (2005).

Measurements were performed in a closed-loop wind tunnel, the test–section of which is 21.6 m in length (along x), 1 m high (along y) and 2 m wide (along z). The boundary layer develops along the flat lower wall of the wind tunnel which has a constant cross-section. Consequently, a small pressure gradient exists which has been quantified. The longitudinal axis x is parallel to the wall and to the mean flow, y is the axis normal to the wall and the transverse axis is z. The instantaneous velocity components u, v and w are associated to the x-, y- and z-axis, respectively. The u_i, x_i notation will also be used in the present contribution; u_i will be the instantaneous velocity component, $\overline{u}_i$ the mean value and u_i' the fluctuation.

For hot-wire anemometry, probes of boundary-layer type, with a diameter of 2.5 μm and a length of 0.5 mm were employed by Carlier (2001) to investigate in detail the turbulent characteristics of the flow. Constant temperature anemometers (AALab Systems) were used to drive the hot-wires. The sampling frequency F_{acq} and the cutting frequency F_c of the low-pass filter were chosen on the basis of an estimation of the Kolmogorov scales to ensure a proper resolution of all temporal scales (see Carlier & Stanislas 2005 for details).

The stereoscopic PIV measurements were carried out by Kähler *et al.* (2000) and are available in the WALLTURB database. They were recorded with a 2×330 mJ BMI ND-YAG laser, with two synchronized PCO cameras (CCD array of 1024×1280 pixels) mounted in an angular configuration with Scheimpflug correction. The interrogation window size used for the fast-Fourier-transform-based free-shape cross-correlation analysis of images was 32×32 pixels with 50% overlap. The main characteristics of the two PIV experiments that were performed are summarized in table 1. The spatial resolution given in this table is the grid spacing. It should be noted here that, as a difference from the results of Carlier & Stanislas (2005), the

Re_θ	7800	15 000
Field of view	$750^+ \times 492^+$ $93 \times 61\,\text{mm}^2$	$1\,631^+ \times 1\,070^+$ $93 \times 61\,\text{mm}^2$
Spatial resolution	$5.4^+ \times 5.4^+$ $0.66 \times 0.66\,\text{mm}^2$	$11.6^+ \times 11.6^+$ $0.66 \times 0.66\,\text{mm}^2$
Number of fields	2940	2100
Number of vectors per field	141×93	141×93

TABLE 1. PIV experiments characteristics.

U_e (m s^{-1})	P, x (Pa m^{-1})	u_τ (m s^{-1})	u^* (m s^{-1})	δ (m)	δ^+ –	θ (m)	Re_θ –	l^+ –	d^+ –
3	−0.065	0.115	0.111	0.35	2 680	0.041	8 171	4.	0.02
5	−0.151	0.183	0.184	0.32	3885	0.034	11 454	6.	0.03
7	−0.247	0.249	0.252	0.30	4 941	0.031	14 505	8.5	0.04
10	−0.528	0.354	0.348	0.30	7 164	0.031	20 831	12	0.06

TABLE 2. Turbulent boundary-layer characteristics: U_e, external velocity; P, x, streamwise pressure gradient; u_τ, wall friction velocity from macroPIV (Foucaut *et al.* 2006); u^*, wall friction velocity from Clauser plot; δ, boundary-layer thickness; $\delta^+ = \delta.u_\tau/\nu$; θ, boundary-layer momentum thickness; $Re_\theta = U_e\theta/\nu$, Reynolds number based on momentum thickness; l^+, length of hot wires in wu d^+diameter of hot wires in wu.

fields of view retained in the present study cover most of the logarithmic layer, for both Reynolds numbers. It should also be noted that the field of view in physical units was kept constant in these experiments. Consequently, the spatial resolution in wall units is different in both cases. From table 1 and based on the Nyquist criterion, we can expect to resolve, at best, vortices of 10 and 20 wall units in diameter at $Re_\theta =$ 7800 and 15 000, respectively.

3. Hot-wire anemometry

Although the hot-wire data have already been presented in Carlier & Stanislas (2005), some new information on the wall friction has been made available since then, which justifies revising them. The estimation of the pressure gradient was also slightly improved, together with the different integral thicknesses. Besides, for the purpose of the present analysis, it is of interest to look at higher-order moments and at dissipative scales which were not shown by these authors.

Carlier & Stanislas (2005) obtained the wall friction velocity u^* with an accuracy of the order of 2% from a Clauser plot of the log layer of the velocity profile, using $\kappa = 0.41$. Foucaut, Stanislas & Kostas (2006) measured the skin friction (and thus the friction velocity u_τ) at the same location and for the same Reynolds numbers using a macroPIV method. The accuracy of the macroPIV measurements is of the order of 1% on the friction velocity at the three lowest Reynolds numbers and of 1.5% at the highest one.

The main characteristics of the boundary layer are summarized in table 2. The kinematic viscosity was $\nu = 15.0 \times 10^{-6}\,\text{m}^2\,\text{s}^{-1}$ for all four cases thanks to the temperature regulation of the wind tunnel. For the sake of simplicity, test cases will be referenced by their rounded Reynolds numbers (i.e. 8200, 11 500, 14 500 and 20 800) in the following. Table 2 gives also the length l and diameter d of the hot wires used (respectively, 0.5 mm and 2.5 μm) in wall units. The spatial resolution can

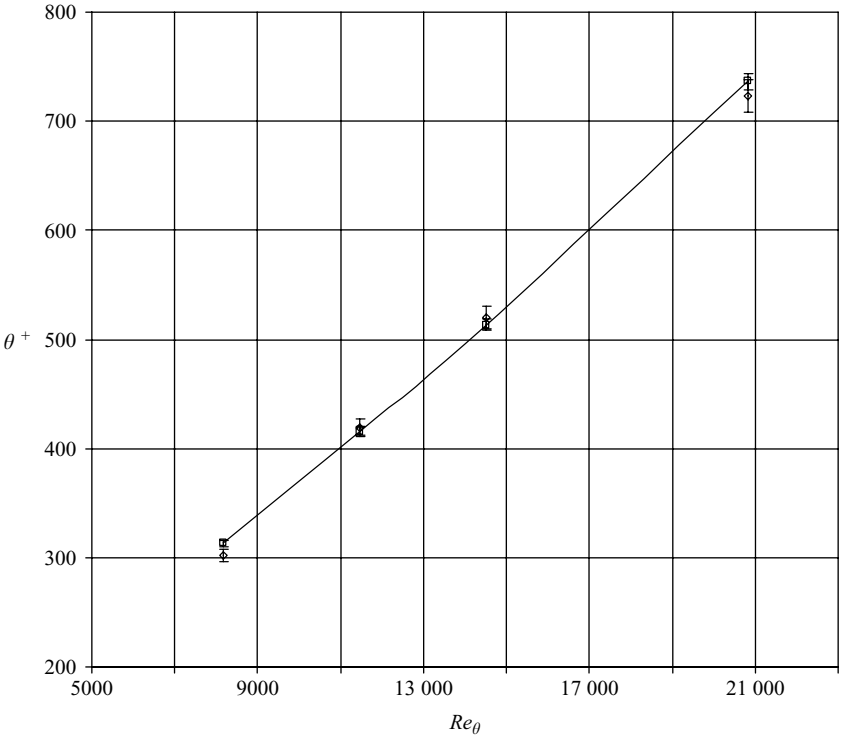

FIGURE 1. θ^+ as a function of Re_θ. Comparison between friction velocity u^* ($\diamond$) deduced from the Clauser plot with $\kappa = 0.41$ and u_τ ($\square$)deduced from macro PIV measurements near the wall.

be deduced from these data and compared with that of PIV in table 1 for both single and cross hot-wire measurements.

Figure 1, by plotting θ^+ ($= u_\tau \theta/\nu$ or $u^* \theta/\nu$) as a function of $Re_\theta = U_e\theta/\nu$, compares the two estimations of the friction velocity, u_τ and u^*. The error bars are 1% for the PIV measurements and 2% for the Clauser plot using $\kappa = 0.41$. The agreement is within the uncertainty, except at the lowest Reynolds number. This should be attributed to the estimation of u^*, as this velocity profile is not the best of the three near the wall, probably owing to some influence of free convection and the difficulties in calibrating hot wires at the lowest velocities (less than $1\,\mathrm{m\,s^{-1}}$). Nevertheless, the agreement is fairly good and gives some confidence in the estimation of u_τ for later scaling.

The mean velocity profiles are not plotted again. They are provided in Carlier & Stanislas (2005) and do not change significantly when using u_τ instead of u^* for scaling.

Figure 2 gives the pressure coefficient $Cp = P/(1/2)\rho U_e^2$ along the wind tunnel (symbols) together with the fit performed to estimate the pressure gradient (lines). The slope of the lines gives the effective pressure gradient. The values are slightly different from Carlier & Stanislas (2005) as here the first two points at the entrance of the test section were not taken into account to make the fit, as they appear to be slightly influenced by the upstream contraction. As can be seen, in most of the wind tunnel, the pressure gradient can be considered as constant. The level of this pressure gradient has already been shown to be fairly small (Carlier & Stanislas 2005).

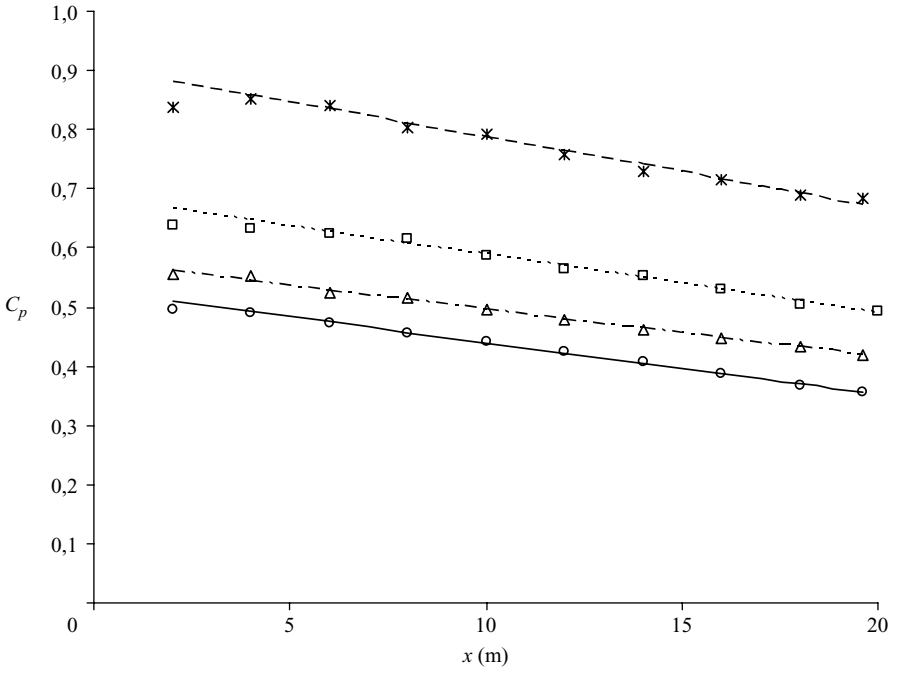

FIGURE 2. Pressure distribution along the wind tunnel at four values of external velocity: $3\,\mathrm{m\,s^{-1}}$(∗); $5\,\mathrm{m\,s^{-1}}$(□); $7\,\mathrm{m\,s^{-1}}$(△); $10\,\mathrm{m\,s^{-1}}$(○); lines correspond to the pressure gradient estimation given in table 2.

Figures 3 and 4 show, respectively, the skewness and flatness factors, in wall scaling (u_τ, ν) and logarithmic representation. Apart for the lowest Reynolds number, which shows slightly different values of skewness (probably due to the lower value of Re_θ), these two parameters appear fairly universal in both the near-wall and the external regions, using the corresponding scaling. Both are fairly constant in the log layer, with respective values near 0 and 3 corresponding to the Gaussian standards. In the wake region, the intermittency is clearly visible. The very near-wall behaviour is of interest. Near the wall, measurements of both parameters start from high positive values, indicating strong intermittency. They decrease very rapidly, showing both a minimum which is at $y^+ \simeq 30$ for $S(u)$ and $y^+ \simeq 13$ for $F(u)$. A small maximum appears at $y^+ \simeq 120$ for $S(u)$ and $y^+ \simeq 50$ for $F(u)$. Putting aside the viscous sublayer and the log layer which show monotonous behaviour, it is clear from these figures that the buffer layer is a place of very strong and rapid changes in the physics of the flow.

In order to perform a proper scaling of the different quantities analysed in the present study, it is of interest to look at the dissipation rate of turbulent kinetic energy ϵ and at the corresponding length scales. There are different ways of estimating ϵ from hot-wire measurements (Pope 2000). Owing to the characteristics of the hot-wire signal (measurement noise), these methods are not equivalent. Some of them were tried here. The method using the dissipation spectrum ($\epsilon = 15\nu \int_0^\infty E_{11} k^2 \,\mathrm{d}k$) does not work well because the multiplication by k^2 amplifies the high-frequency noise. The one based on the time derivative of the velocity fluctuations does not work either, owing to the transfer function of the derivative filter (this has been studied in detail for PIV by Foucaut *et al.* 2004). The method based on $\epsilon = 30\nu(u'(y))^2/\lambda_1(y)$ (with $\lambda_1(y)$

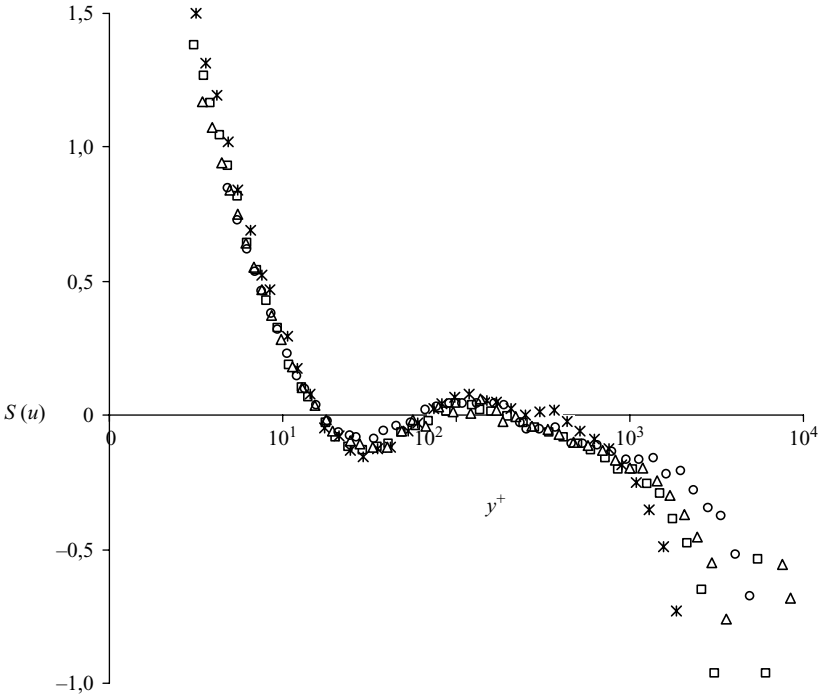

FIGURE 3. Wall-normal evolution of the skewness factor $S(u)$ in log inner scaling. $Re_\theta =$ 8200 (∗); $Re_\theta = 11\,500$ (□); $Re_\theta = 14\,500$ (△); $Re_\theta = 20\,800$ (○).

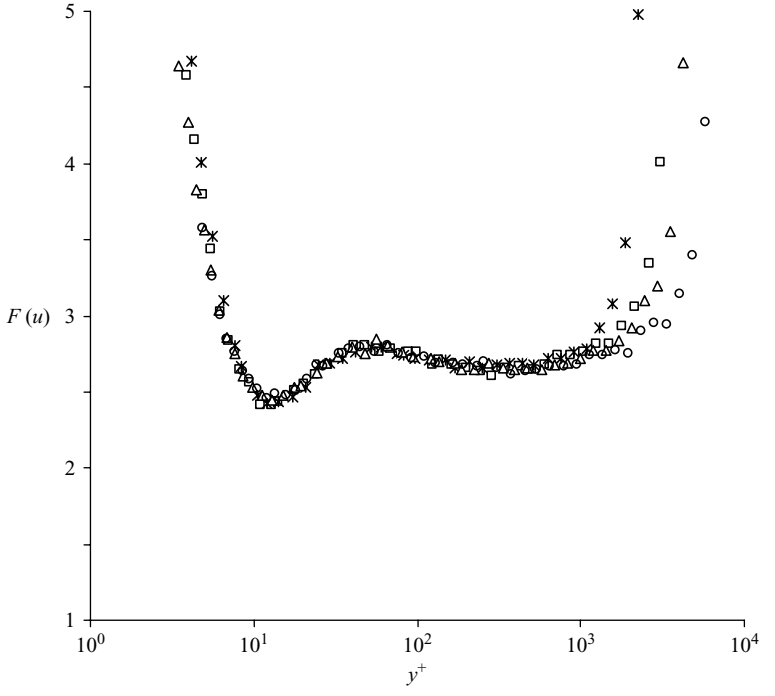

FIGURE 4. Wall-normal evolution of the flatness factor $F(u)$ in log inner scaling. $Re_\theta = 8200$ (∗); $Re_\theta = 11\,500$ (□) $Re_\theta = 14\,500$ (△) $Re_\theta = 20\,800$ (○).

being the Taylor micro scale of the streamwise velocity component) was retained. The Taylor microscale is defined as:

$$\lambda_1(x) = \sqrt{\frac{-2}{\left.\dfrac{\partial^2 R_{11}(x, x+\mathrm{d}x)}{(\partial\,\mathrm{d}x)^2}\right|_{\mathrm{d}x=0}}}, \tag{3.1}$$

where $R_{11}(x, \mathrm{d}x)$ is the correlation coefficient between the velocity fluctuation components $u'(x)$ and $u'(x + \mathrm{d}x)$. A local Taylor hypothesis, based on the local mean velocity of the flow is employed to compute λ_1 directly from the temporal correlation coefficient. The second-order derivative involved in (3.1) is computed via a fourth–order centred scheme. With this method, the noise, which is incoherent, affects only $R_{11}(x, x + 0)$ and does not perturb the estimation of λ_1.

The distribution of ϵ across the boundary layer is plotted in figure 5 both in mixed ($\epsilon\delta/u_\tau^3$) and wall ($\epsilon\nu/u_\tau^4$) scalings. As expected, the peak of ϵ is at the wall. The dissipation decreases very rapidly with wall distance, with most of it occurring in the viscous and buffer layers. In these two figures are also plotted for comparison the data of Hoyas & Jimenez (2006) from a channel flow DNS at $Re_\tau = u_\tau h/\nu = 2003$ (with $h \simeq \delta$). A fairly good agreement is obtained in mixed representation and a certain degree of universality develops when the Reynolds number is high enough (Re_θ above 11 500). In wall unit representation, the dissipation is obviously Reynolds-number dependent and the agreement is not so good between experiments and DNS (in particular, very near to the wall). This can be explained by two facts: (i) The method used to determine ϵ is fairly different. In DNS the full expression of ϵ is used directly whereas in the experiment, this quantity is determined from the fluctuations of one single velocity component, on the basis of an isotropy hypothesis. (ii) The Reynolds number of the DNS is lower than in the experiments. Although δ^+ is not so different from R_τ (2680 for the lowest boundary-layer (BL) Reynolds number compared to 2003 for the DNS), the ratio U_c/u_τ is 2.43 in the DNS while U_e/u_τ is 27 at the lowest Reynolds number of the experiments. It is difficult to quantify the relative contribution of these two sources of bias, but at least the results are coherent and the experimental results which will be used later are determined with the same method.

The wall-normal evolution of λ_1, from which ϵ is computed, is given in wall units in figure 6(a). This parameter shows a slight Reynolds-number dependence in this representation. This dependence is much stronger when plotted in external units ($\lambda_1/\delta = f(y/\delta)$, not shown). Here, the near-wall region can be divided roughly into: $y^+ < 10$; $10 < y^+ < 100$; $100 < y^+$. In the intermediate 'buffer layer', where the rapid changes in $S(u)$ and $F(u)$ occur, this micro scale appears fairly constant. In the two other regions, a monotonous increase with wall distance is observed, with a global variation of about one order of magnitude over the whole BL thickness.

From the dissipation, the Kolmogorov length scale η can be estimated as $\eta = (\nu^3/\epsilon)^{1/4}$. Figure 6($b$) shows the wall-normal evolution of η scaled in wall-units for both Reynolds numbers. This quantity exhibits good universality in the region investigated and compares well, in the logarithmic region, with the power law $\eta^+ = (\kappa y^+)^{1/4}$ (where $\kappa = 0.41$ is the Kármán constant) resulting from the balance between production and dissipation (Pope 2000). This length scale does not show universality in external scaling (not shown).

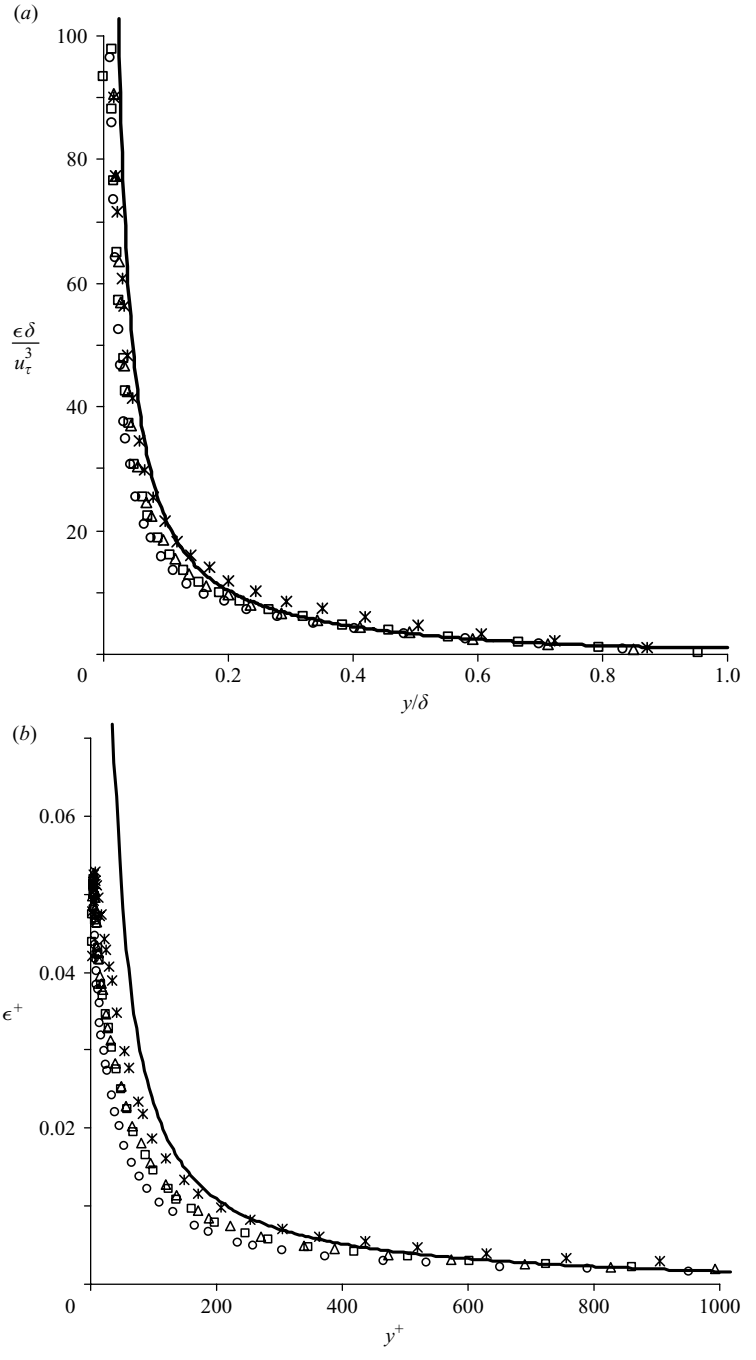

FIGURE 5. Wall-normal evolution of the dissipation ϵ in (*a*) external and (*b*) inner scaling. $Re_\theta = 8200$ (∗); $Re_\theta = 11\,500$ (□); $Re_\theta = 14\,500$ (△); $Re_\theta = 20\,800$ (○); DNS $Re_\tau = 2\,000$ (Hoyas & Jimenez 2006) (—).

4. Statistical analysis of swirling motion

The proposed statistical analysis of the swirling motion existing in the (y, z)-plane is based on the use of the swirling strength λ_{ci}. It is shown by Zhou *et al.* (1999),

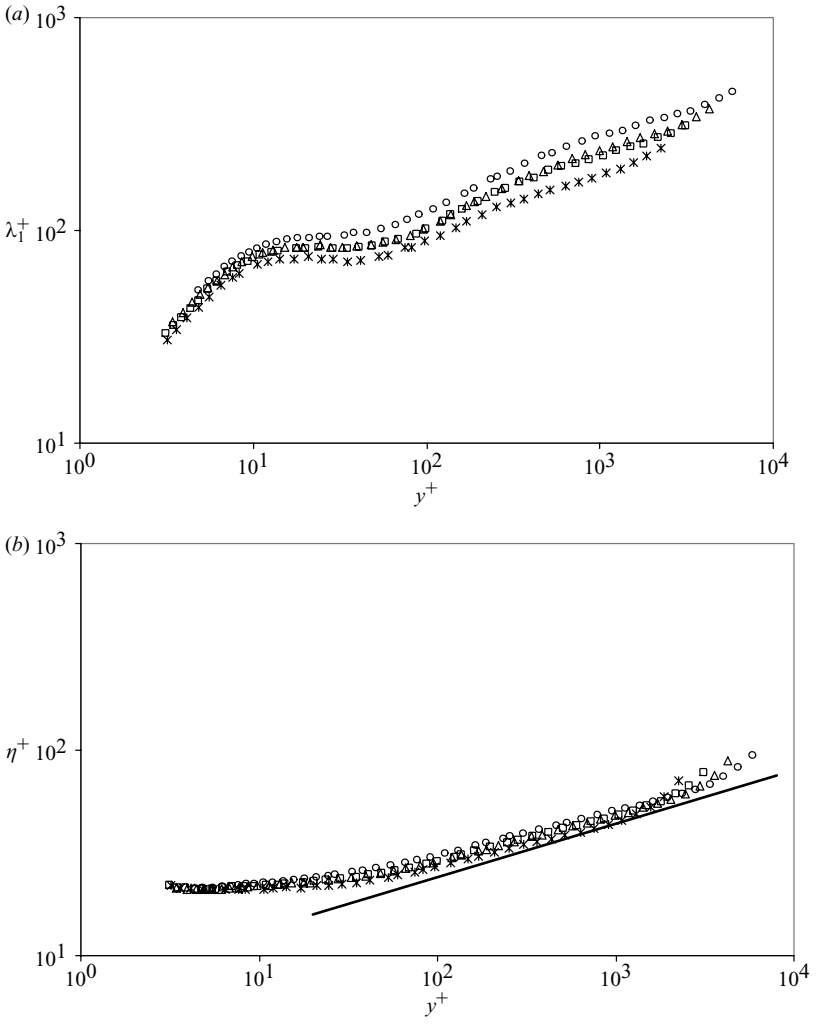

FIGURE 6. Wall-normal evolution of (*a*) the Taylor microscale of the longitudinal velocity λ_1^+ and (*b*) the Kolmogorov scale η^+ at $Re_\theta = 8200$ (∗); $Re_\theta = 11\,500$ (□); $Re_\theta = 14\,500$ (△); $Re_\theta = 20\,800$ (○).

Adrian *et al.* (2000*a*) and Chakraborty *et al.* (2005) that λ_{ci}, which is the imaginary part of the complex eigenvalue of the velocity gradient tensor, is an efficient vortex core identification criterion. As proposed by Tomkins & Adrian (2003) and Hutchins *et al.* (2005), λ_{ci} is here multiplied by the sign of the streamwise vorticity component ω_1. Thus, $\lambda_s = \lambda_{ci}\omega_1/|\omega_1|$ is formed to discriminate counter-clockwise rotating vortices ($\lambda_s > 0$) from clockwise ones ($\lambda_s < 0$). Hutchins *et al.* (2005) demonstrated that this criterion, computed from a two-dimensional velocity field, can successfully detect vortex cores cutting the measurement plane, even at an oblique angle. Thus, analysis of the swirling strength in the (y, z)-plane is expected to provide reliable information on hairpin vortex legs. In the present study, velocity gradients are computed by using a second-order centred difference scheme which presents a transfer function comparable to the PIV one (Foucaut *et al.* 2004). Only results obtained at $Re_\theta = 7800$ are presented in this section.

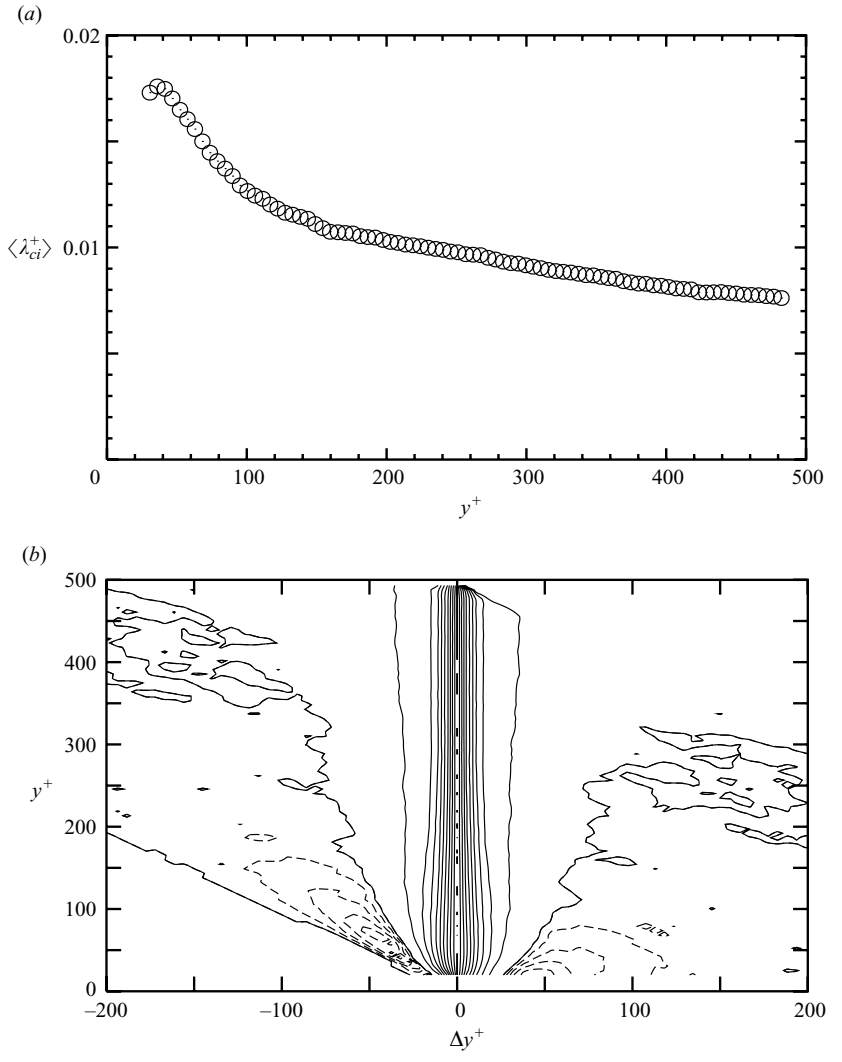

FIGURE 7. Wall-normal evolution of (*a*) mean swirl λ_{ci}^+ and (*b*) spatial correlation of signed swirling strength, $R_{\lambda_s\lambda_s}(y^+, \Delta y^+, \Delta z^+ = 0)$; (solid) positive contours from 1 (on the $\Delta y^+ = 0$ axis) to 0 in decrements of 0.1, (dashed) negative contours from 0 to -0.04 in decrement of 0.01, at $Re_\theta = 7800$.

4.1. *Wall-normal organization*

Wall-normal evolution of the mean swirling strength $\langle\lambda_s^+\rangle$, where $\langle.\rangle$ denotes the ensemble-averaging operator both in the homogeneous z-direction and over all the acquired velocity fields, is shown in figure 7(*a*). The flow exhibits a strong streamwise oriented swirling activity in the near-wall region (e.g. for $y^+ < 100$ to 150), which then decays slowly with the distance from the wall. These results are in good agreement with those of Hutchins *et al.* (2005) and those from Carlier & Stanislas (2005) who detected vortices in a plane inclined at an angle of 45° upstream by using a pattern-recognition technique. They confirm that the two-dimensional swirling strength in the (y, z)-plane correctly captures the vortices related to the coherent structures of the turbulent boundary layer.

In order to analyse in more detail the vortex organization, following Christensen & Adrian (2001) and Wu & Christensen (2006), the two-point correlation tensor of the signed swirling strength is computed as:

$$R_{\lambda_s\lambda_s}(y, \Delta y, \Delta z) = \frac{\langle \lambda_s(y, z)\lambda_s(y + \Delta y, z + \Delta z)\rangle}{\sigma_{\lambda_s}(y)\sigma_{\lambda_s}(y + \Delta y)}, \tag{4.1}$$

where σ is the r.m.s. of the given quantity. If the coherent structures present in the flow show any spatio-temporal organization of statistical importance, this organization should leave its imprint on the two-point statistics.

Figure 7(b) illustrates $R_{\lambda_s\lambda_s}$ obtained for $\Delta z = 0$, at $Re_\theta = 7800$. The correlation pattern is dominated by a narrow central peak of quasi-constant width at $\Delta y = 0$, $\forall y$, which corresponds to the presence of a single vortex. Negative correlation levels, comprised between 0 and 5%, can be observed in the region $y^+ < 150$. Vortices located in this region are weakly correlated with counter-rotating vortices located above them ($\Delta y^+ > 0$). In the same manner, correlation also exists between vortices of this region with counter-rotating eddies located below them. Thus, two regions can be distinguished, one, for $y^+ < 150$, of stronger interaction between vortices and strong swirling activity and another above, where vortices appear to be more isolated from a statistical point of view. In order to analyse in more detail the shape of this correlation, it was computed with a condition on the sign of the swirling strength. Figure 8 shows the same correlation as in figure 7(b), but conditioned on the sign of the swirling strength. Figure 8(a) gives:

$$R_{\lambda_s\lambda_s} \text{ for } \lambda_s(y, z)\lambda_s(y + \Delta y, z + \Delta z) > 0,$$

while figure 8(b) gives:

$$R_{\lambda_s\lambda_s} \text{ for } \lambda_s(y, z)\lambda_s(y + \Delta y, z + \Delta z) < 0.$$

In figure 8(a), only one peak is visible at $\Delta y = 0$, indicating no correlation between vortices of the same sign in the wall normal direction in the whole field of investigation. Moreover, the nearly constant width of this peak along y is remarkable and indicative of the nearly constant size of these structures. This result is in good agreement with the findings of Carlier & Stanislas (2005) using pattern-recognition methods. In figure 8(b), the negative correlation areas above and under the reference vortex are more visible, indicating clearly that counter–rotating vortices can be found both above and under the reference vortex. The local extrema observed on both sides of $\Delta y^+ = 0$ seem to indicate that when a vortex is travelling under $y^+ = 150$, there is a higher chance that a counter-rotating one forms near the wall under it. This result supports the idea of new vortices developing near the wall along the legs of an hairpin (Adrian 2007).

Figures 9 shows profiles of the correlation map of figure 7(b), obtained at constant y^+ to look in more detail at the shape of the correlation tensor. Negative levels indicate the statistical predominance of interactions between counter-rotating vortices. In the present case, as $\Delta z^+ = 0$, counter-rotating vortices would be located one above the other. Therefore, its seems obvious that these pairs of vortices are not part of the same hairpin–shaped structure, but rather-distinct coherent structures interacting in the near-wall region. They can be linked to the packets of vortices found by several workers along low-speed regions (Ganapathisubramani *et al.* 2003; del Álamo *et al.* 2006).

As can be seen in figure 7(b) and more clearly in figure 9(b), spatial organization in the y-direction of the in-plane swirling motion is clearly different below and above

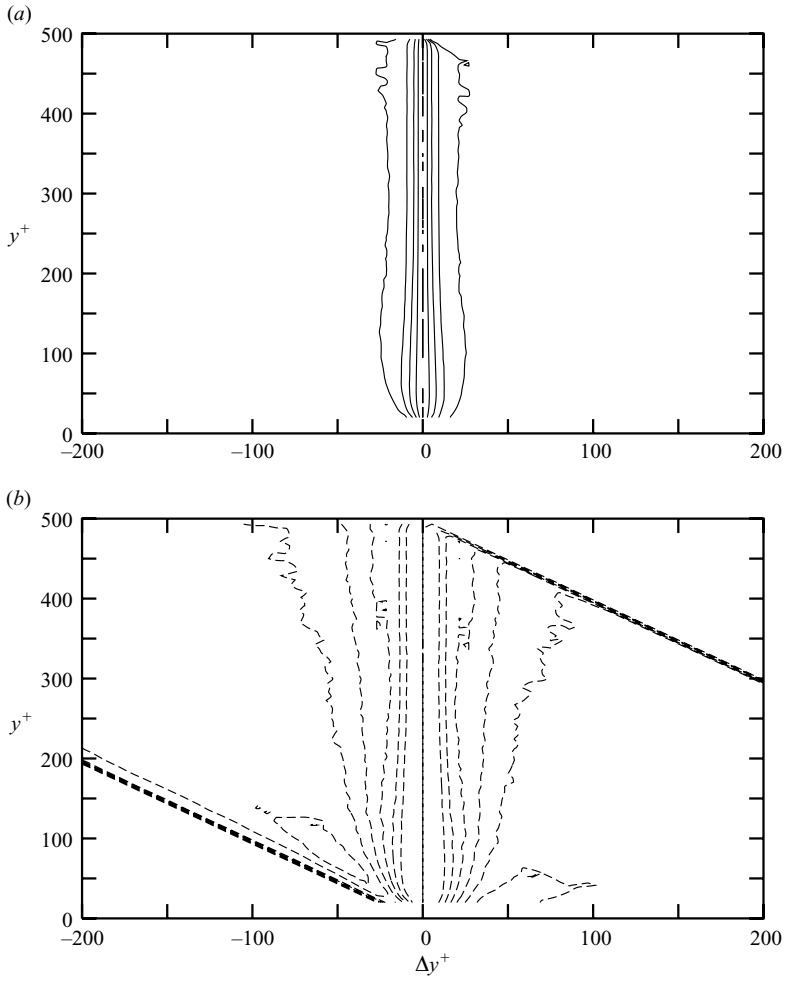

FIGURE 8. Spatial correlation of the signed swirling strength, $R_{\lambda_s\lambda_s}(y^+, \Delta y^+, \Delta z^+ = 0)$, conditioned by the sign of the swirling events: swirling events of (*a*) the same sign and (*b*) of opposite signs at the reference point and the moving point, at $Re_\theta = 7800$. Contour levels and increments and line type are the same as in figure 7, except for the lowest level being -0.07.

$y^+ = 150$. The statistical imprint of the interaction of counter–rotating vortices is no longer present in $R_{\lambda_s\lambda_s}$ above $y^+ = 150$. Only one peak of self-correlation can be seen, corresponding to the statistical dominance of a single vortex of streamwise vorticity. The evolution of the shape of the correlation profiles, which exhibit two slight secondary 'plateau' located on each side of the correlation maximum, may be attributed to a change in shape of the vortices. However, this point remains to be further investigated.

4.2. *Spanwise organization*

Profiles of the spatial correlation $R_{\lambda_s\lambda_s}$ as a function of the spanwise separation Δz^+, at various wall-normal locations y^+ and for zero wall-normal separation ($\Delta y^+ = 0$) are illustrated in figure 10(*a*). It should be noted here that the symmetry of the correlation tensor in the spanwise direction is due to the homogeneity of the

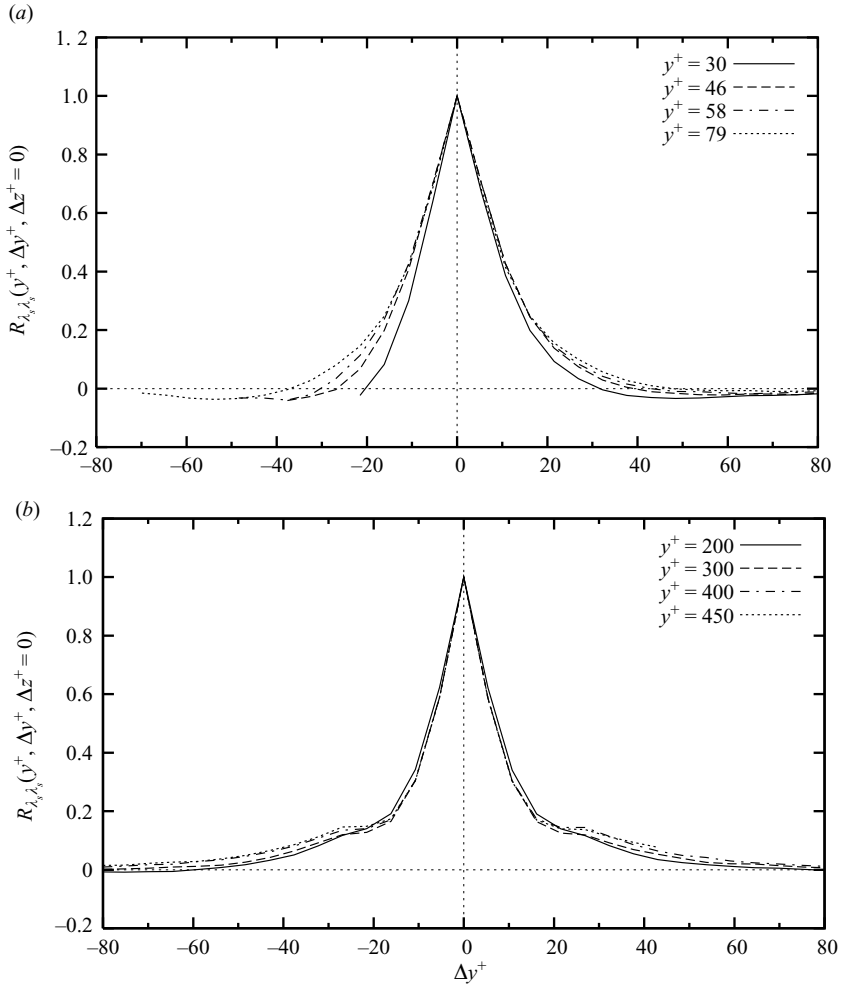

FIGURE 9. Profiles of spatial correlation of signed swirling strength, $R_{\lambda_s\lambda_s}(y^+, \Delta y^+, \Delta z^+ = 0)$ for (*a*) $y^+ = 30$, 46, 58 and 79 and (*b*) $y^+ = 200$, 300, 400 and 450, at $Re_\theta = 7800$.

flow in this direction and does not reflect any particular symmetry of the coherent structures. Again, the shape of the correlation profiles varies with the wall-normal location considered. Below $y^+ \simeq 150$, negative extrema of correlation exist on each side of the self-correlation peak, the level of which is less than 5%. This negative correlation is indicative of counter-rotating vortices beside the reference one in the near-wall region. The spanwise distance between the central peak and a negative extremum is approximately 50 wall-units at $y^+ = 50$. This distance corresponds well to the spanwise spacing of counter-rotating vortices found by Hutchins *et al.* (2005) in their conditional analysis of swirling motion at the same height. Moreover, this is consistent with the 'low-speed streaks' width computed for $y^+ \leqslant 50$ by Stanislas *et al.* (2005) (see also Lin 2006) in their experimental study based on PIV measurements in streamwise–spanwise planes at similar Reynolds number. Thus, this result is in agreement with the picture of hairpin vortices consisting of two legs, located on each side of a low-momentum region. However, the low level of correlation supports the idea that hairpin-shaped structures are predominantly asymmetric structures, as

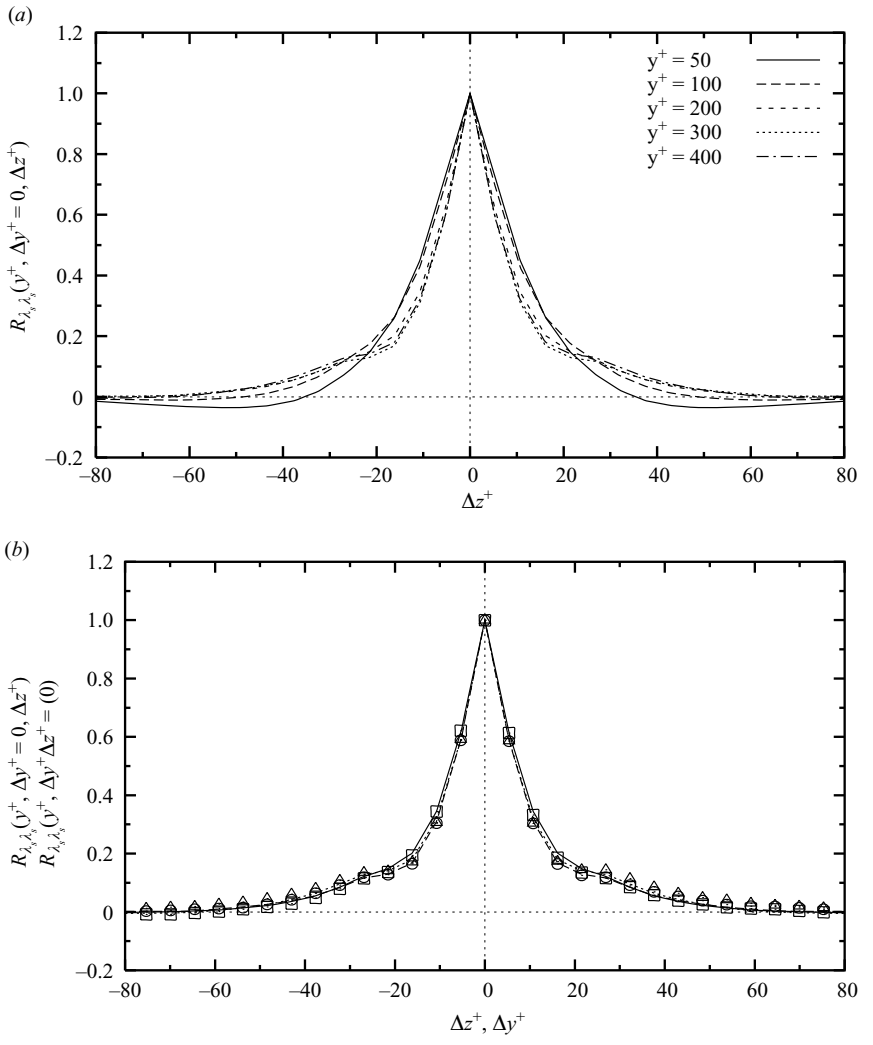

FIGURE 10. Profiles of spanwise correlation of signed swirling strength (*a*) $R_{\lambda_s\lambda_s}(y^+, \Delta y^+ = 0, \Delta z^+)$ at $y^+ = 50$, 100, 200, 300, 400 and (*b*) (line) $R_{\lambda_s\lambda_s}(y^+, \Delta y^+ = 0, \Delta z^+)$ and (symbol) $R_{\lambda_s\lambda_s}(y^+, \Delta y^+, \Delta z^+ = 0)$ at $y^+ = 200$ (—- and □), 300 (- - - and ○), and 400 (· · · and △); $Re_\theta = 7800$.

found by Choi & Guezennec (1989), Guezennec *et al.* (1989) and Robinson (1991) in DNS of low- Reynolds-number wall-bounded flow. For $y^+ \geqslant 100$, inspection of the correlation patterns (not shown here) at larger spanwise separation exhibited no particular organization ($R_{\lambda_s\lambda_s}$ is zero for $\Delta z^+ \geqslant 100$). This point is consistent with the picture of asymmetric vortices.

In the region located above the buffer layer, profiles of $R_{\lambda_s\lambda_s}(\Delta z^+ = 0)$ show the same shape as found for $R_{\lambda_s\lambda_s}(\Delta y^+ = 0)$. Secondary peaks of positive correlation, at $\Delta z^+ \simeq 25$ on each side of the central peak are retrieved, indicating that this length scale is statistically characteristic of the vortex core size. This is confirmed by the fact that, in this region, the correlation tensor exhibits good isotropy: profiles of $R_{\lambda_s\lambda_s}(y, \Delta y, \Delta z = 0)$ match closely those of $R_{\lambda_s\lambda_s}(y, \Delta y = 0, \Delta z)$ (figure 10*b*).

4.3. *One-point LSE of a swirling event*

The conditional velocity field in the (y, z)-plane, given a swirling event of streamwise vorticity at a reference point is estimated here using the linear stochastic estimation (LSE) (Adrian & Moin 1988). In this case, the conditional velocity field $\langle u_i(y_{ref} + \Delta y, \Delta z)|\lambda_s(y_{ref}, 0)\rangle$ is approximated in a linear fashion by

$$\langle u_i(y_{ref} + \Delta y, \Delta z)|\lambda_s(y_{ref}, 0)\rangle \simeq L_i \lambda_s(y_{ref}, 0), \tag{4.2}$$

where

$$L_i = \frac{\langle u_i(y_{ref} + \Delta y, \Delta z)\lambda_s(y_{ref}, 0)\rangle}{\langle \lambda_s(y_{ref}, 0)^2\rangle} \tag{4.3}$$

is derived from the minimization of the mean-square error between the estimate and the conditional average. As the one-point conditional event LSE is simply a function of the two-point correlation tensor, the spatial structure of the estimate does not depend on the intensity of the conditional event and a change of sign of the reference signal will result only in a change of sign of the estimated field.

Figure 11 shows the velocity field estimated by LSE at two reference heights $y^+_{ref} = 50$ and 300. In both cases, the estimate associated to a positive swirling strength event depicts a counter-clockwise rotating vortex core, the axis of which is more or less normal to the investigated plane, bordered by low- and high-momentum regions on the right- and left-sides respectively. This picture is fully consistent with an asymmetric hairpin structure and with the mean picture obtained by Carlier & Stanislas (2005) with conditional pattern-recognition techniques. If the most probable vortex organization was a more or less symmetric hairpin, and according to the flow homogeneity in the spanwise direction, we would have expected three counter-rotating vortex cores, one on each side of the central vortex, symmetrically distributed along the z-direction. Thus, the estimated conditional velocity field seems to support the idea that statistically predominant vortical structures in the turbulent boundary layer are 'one-legged' hairpins or 'cane' vortices. It also implies that interactions between counter-rotating vortices found in previous sections (figures 9*a* and 10*a*) in the near-wall region for $y^+ < 150$ are not statistically significant in a least-squares sense.

Besides, figures 11(*a*) and 11(*c*) clearly show that swirling events are linked to regions of low- and high-streamwise velocity. This is particularly marked near the wall and much more loose in the log layer. The dominant spatio-temporal organization corresponding to these results is, for instance, counter-clockwise rotating ($\lambda_s > 0$) vortices bordering a low-momentum region located on their right-hand side and clockwise rotating ($\lambda_s < 0$) vortices with low momentum region on their left-hand side, when looking in the $x > 0$ direction. This is in good agreement with the findings of Tomkins & Adrian (2003). In spite of the lower statistical convergence of the correlation at large Δz, the correlation length associated to a given correlation level increases as the reference point moves away from the wall. Thus, vortices are obviously associated with wider and wider regions of coherent longitudinal velocity with increasing wall-distance, consistently with the structure and scale growth found in the spanwise direction by Tomkins & Adrian (2003) and Ganapathisubramani *et al.* (2005).

Conversely, it appears that the characteristic size of the vortex core evolves less rapidly with the wall-normal distance than the width of the regions of constant longitudinal velocity. To clarify this point, the radius of the vortex associated to the linear estimates has been computed by fitting an Oseen vortex model (see (4.4)) to

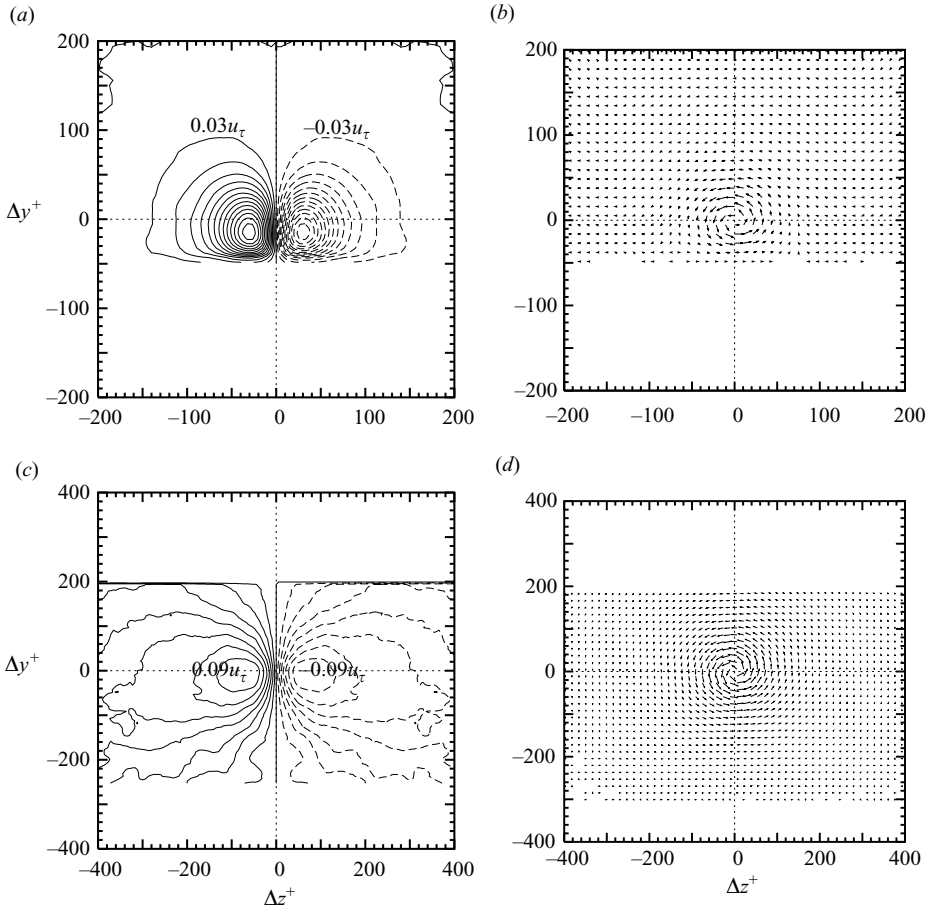

FIGURE 11. One-point linear stochastic estimation of the velocity field in the (y, z)-plane conditioned by a positive swirling strength event of magnitude $\langle \lambda_{ci}(y_{ref}) \rangle$ located at (a, b) $y^+_{ref} = 50$ and (c, d) $y^+_{ref} = 300$. Contours (a, c) show conditioned streamwise velocity in increment of (a) $0.03u_\tau$ and (c) $0.013u_\tau$ (negative contours are dashed); $Re_\theta = 7800$.

the estimated velocity field in the (y, z)-plane:

$$\boldsymbol{u}(\boldsymbol{r}) - \boldsymbol{u}_0(\boldsymbol{x}_0) = \frac{\Gamma_0}{2\pi r}\left[1 - \exp - \left(\frac{r}{r_0}\right)^2\right] \cdot \boldsymbol{e}_\theta, \tag{4.4}$$

where $\boldsymbol{u}$ is the velocity vector in the (y, z)-plane, $\boldsymbol{r} = \boldsymbol{x} - \boldsymbol{x}_0$ is the position vector in this plane, r is the modulus of $\boldsymbol{r}$ and $\boldsymbol{e}_\theta$ is the tangential unit vector in polar coordinates. The circulation Γ_0, the radius r_0, the position vector of the centre $\boldsymbol{x}_0$ and the convection velocity $\boldsymbol{u}_0$ are the fitted parameters of the model. The vorticity at the eddy centre is calculated as $\omega_0 = \Gamma_0/(\pi r_0^2)$. Figure 12 shows the evolution of the estimated radius as a function of the wall-normal distance. As found by Carlier & Stanislas (2005), the mean radius of the vortices slowly increases for $y^+ > 100$, consistently with the analysis of $R_{\lambda_s \lambda_s}$ performed in § (4.2). The value of this radius is also in fair agreement with previous studies.

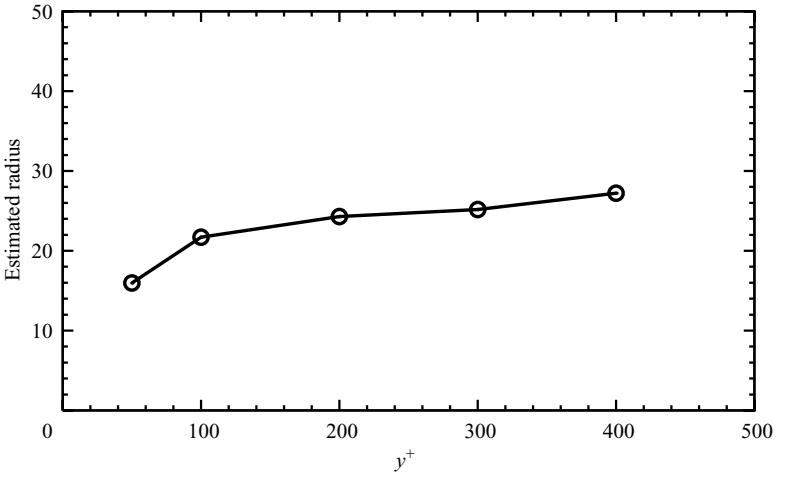

FIGURE 12. Radius r_0^+ of the conditional vortex core obtained by LSE in the (y, z)-plane as a function of the wall-normal location; $Re_\theta = 7800$.

4.4. *Two-point LSE*

Given the strong correlation level that exists between a swirling event and regions of coherent (high or low) streamwise velocity near the wall (see figure 11*a*) and to overcome the fact that the spanwise homogeneity of the flow can hide some specific features of the coherent structures, relationships between a vortical event and a region of coherent streamwise velocity are now investigated via a two-point linear stochastic estimation approach. The formalism of the linear stochastic estimation allows one to estimate the conditional average of the velocity field under multiple conditions at different locations. In the present case, it is proposed to estimate the velocity field in the plane of measurement when a negative fluctuating streamwise velocity event occurs at $y^+ = 30$ together with a positive swirling strength event at $y^+ = 50$ and $\Delta z^+ = -26$, namely $\langle u_i(y, \Delta z)|u_1(y^u_{ref}, 0), \lambda_s(y^s_{ref}, \Delta z^s_{ref})\rangle$. This corresponds to the presence of a low-speed streak bordered on its left-hand side by a vortical structure, as underlined in figures 11(*a*, *b*). Here, the conditional average $\langle u_i(y, \Delta z)|u_1^{ref}, \lambda_s^{ref}\rangle$ of the velocity field under two conditions u_1^{ref} and λ_s^{ref} is approximated by

$$\left\langle u_i(y, \Delta z)\middle|u_1^{ref}, \lambda_s^{ref}\right\rangle \simeq \widetilde{u_i}(y, \Delta z) = L_i^u u_1^{ref} + L_i^s \lambda_s^{ref}, \tag{4.5}$$

where

$$L_i^u = \frac{\left\langle u_i(y_{ref} + \Delta y, \Delta z)\lambda_s^{ref}\right\rangle\left\langle u_1^{ref}\lambda_s^{ref}\right\rangle - \left\langle u_i(y_{ref} + \Delta y, \Delta z)u_1^{ref}\right\rangle\left\langle \lambda_s^{ref\,2}\right\rangle}{\left\langle u_1^{ref}\lambda_s^{ref}\right\rangle^2 - \left\langle u_1^{ref\,2}\right\rangle\left\langle \lambda_s^{ref\,2}\right\rangle} \tag{4.6}$$

and

$$L_i^s = \frac{\left\langle u_i(y_{ref} + \Delta y, \Delta z)u_1^{ref}\right\rangle\left\langle u_1^{ref}\lambda_s^{ref}\right\rangle - \left\langle u_i(y_{ref} + \Delta y, \Delta z)\lambda_s^{ref}\right\rangle\left\langle u_1^{ref\,2}\right\rangle}{\left\langle u_1^{ref}\lambda_s^{ref}\right\rangle^2 - \left\langle u_1^{ref\,2}\right\rangle\left\langle \lambda_s^{ref\,2}\right\rangle} \tag{4.7}$$

are derived from the minimization of the mean-square error between the estimate and the conditional average. Contrary to the one-point linear estimate, it can be seen that the sign of the chosen conditions plays an important role on the structure of the result.

To obtain the stochastic estimation of the velocity field for a range of reference parameter (swirling strength and longitudinal velocity) values, e.g. $u_1^{ref} < k_u\sigma_u$ and $\lambda_s^{ref} > k_\lambda\sigma_{\lambda_s}$ where k_u and k_λ are some thresholds, u_1^{ref} and λ_s^{ref} in (4.5) are replaced by the appropriate conditional moments deduced from the probability density functions $\mathrm{pdf}(u_1')$ and $\mathrm{pdf}(\lambda_s)$, respectively:

$$\left\langle u_1^{ref} \left| u_1^{ref} < k_u\sigma_u \right.\right\rangle = \frac{\displaystyle\int_{-\infty}^{k_u\sigma_u} u_1^{ref}\,\mathrm{pdf}\left(u_1^{ref}\right)\mathrm{d}u_1^{ref}}{\displaystyle\int_{-\infty}^{k_u\sigma_u} \mathrm{pdf}\left(u_1^{ref}\right)\mathrm{d}u_1^{ref}} \tag{4.8}$$

and

$$\left\langle \lambda_s^{ref} \left| \lambda_s^{ref} > k_\lambda\sigma_{\lambda_s} \right.\right\rangle = \frac{\displaystyle\int_{k_\lambda\sigma_{\lambda_s}}^{+\infty} \lambda_s^{ref}\,\mathrm{pdf}\left(\lambda_s^{ref}\right)\mathrm{d}\lambda_s^{ref}}{\displaystyle\int_{k_\lambda\sigma_{\lambda_s}}^{+\infty} \mathrm{pdf}\left(\lambda_s^{ref}\right)\mathrm{d}\lambda_s^{ref}} \tag{4.9}$$

Thus, linear estimates of the velocity field can be obtained, corresponding to a range of reference events. As proposed by Carlier & Stanislas (2005), negative velocity events of amplitude greater than σ_u are considered to be representative of the presence of a low-speed streak. Consequently, a threshold $k_u = -1$ is retained.

Two values of the threshold $k_\lambda = 0$ and $k_\lambda = 1$ are investigated to analyse the influence of the intensity of the reference vortical event retained to perform the estimation of the velocity field. In the first case, all swirling strength events are retained whereas in the second one, only the strongest ones are considered.

Figures 13(*a*) and 13(*b*) present the two-point linear estimate of the in-plane velocity components obtained for $k_u = -1$, $k_\lambda = 0$ and $k_u = -1$, $k_\lambda = 1$ respectively. In both cases, the obtained velocity field corresponds to a single vortex centred at the location of the reference swirl event, bordering the low-speed region. The combination $k_u = -1$, $k_\lambda = 0$ (figure 13*a*) corresponding to the more general case that can occur (e.g. a low-speed streak bordered by a streamwise vortical structure with no restriction on its intensity) shows that the most representative coherent structure is asymmetric with respect to the vertical axis (corresponding to a cane-shaped vortex). The presence of a stronger vortex ($k_u = -1$, $k_\lambda = 1$, figure 13*b*) does not lead to important modifications of the organization of the estimated flow field. Results obtained from a two-point linear stochastic estimation are then fully consistent with previous results based on the analysis of the two-point correlation tensor and of the one-point linear stochastic estimation and correspond to the cane model of asymmetric vortical structures in the near-wall region as proposed, for example, by Robinson (1991). Figure 14 reproduces figure 4 from Guezennec *et al.* (1989), who analyse the flow structure linked to strong Q2 and Q4 events in a DNS of channel flow at $Re_\tau = 180$. Figure 14(*a*) shows the result obtained with a simple ensemble averaging based on a threshold on Q2. A symmetric vortical structure is clearly evidenced. Figure 14(*b*) shows the same result, but with a condition on the strength of one vortex with respect to the other. The similarity between this pattern and the one shown by figure 13 is clear. Although the size of the structure obtained is not the same, owing to the different approaches used, the educed structure is exactly the same. Moreover, these authors come to the same conclusion as here: this vortex is bordered by a Q2 on its right-hand side and a Q4 on the left.

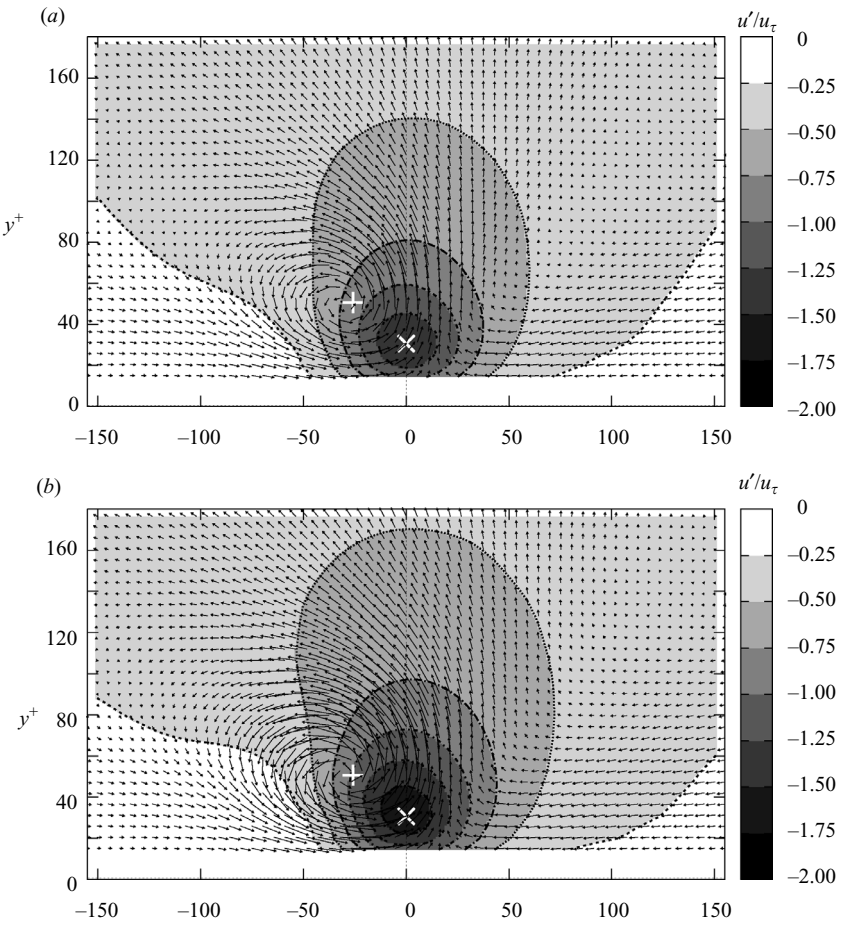

FIGURE 13. Two-point linear estimate of the velocity field in the plane (z, y) with a negative longitudinal velocity event with $k_u = -1$ at $y^+ = 30$, $\Delta z^+ = 0$ ($\times$), and a positive swirling strength event at $y^+ = 50$, $\Delta z^+ = -26$ (+) for (*a*) $k_\lambda = 0$ and (*b*) $k_\lambda = 1$; $Re_\theta = 7800$ (vectors: in-plane velocity components; grey-scale contours: longitudinal velocity component).

5. Vortex extraction

5.1. *Vortex characteristics*

To clarify previous results based on the analysis of the two-point correlation function of the signed swirling strength λ_s and to bring additional quantitative information on the vortices, the eddy-structure validation method implemented by Carlier & Stanislas (2005) is employed here. They proposed to validate the detected vortices (from the computation of a detection function such as vorticity, swirling strength or a pattern-recognition analysis) by fitting an Oseen vortex model (equation (4.4)) to the velocity field surrounding the detection peak (this is very close to the approach of (Das *et al.* (2006)) who fitted a Burgers vortex model to their three-dimensional DNS data). In the present study, the detection function is based on swirling strength maps that have been smoothed by a sliding average filter to eliminate the derivation noise (7×7 and 3×3 for $Re_\theta = 7800$ and 15 000, respectively). Thus, this method allows one to count the vortices existing in the velocity maps of the investigated database and to evaluate their individual position, size and intensity. In this section, results obtained at two

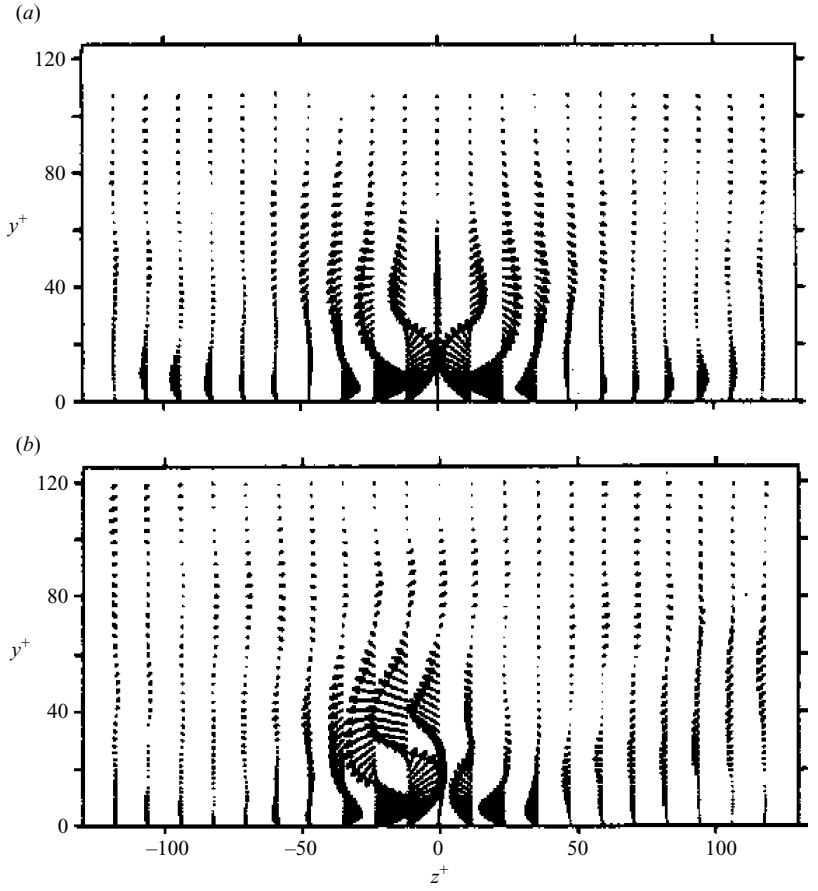

FIGURE 14. Ensemble-averaged structures for the second quadrant event. (*a*) The conventional averaging technique; (*b*) the modified averaging technique. [From Guezennec *et al.* (1989), with permission of *Physics of Fluids* A.]

Reynolds numbers are presented. It should be noted here that, given the fact that the same spatial resolution in physical units has been employed for both Reynolds numbers, velocity fields acquired at the highest Reynolds number $Re_\theta = 15\,000$ are not as well-resolved as those at $Re_\theta = 7800$, when the spatial resolution in wall-units is considered. As shown in table 1, the spatial resolution is of the order of 5 wu at $Re_\theta = 7800$ and 10 wu at $Re_\theta = 15\,000$. This means that vortices smaller than 10 and 20 wu have no chance of being detected. Consequently, based on the results of Carlier & Stanislas (2005) which showed that vortex characteristics scaled in wall-units are almost Reynolds-number independent, statistics of the smaller scales obtained at the highest Reynolds number in the present study will be biased by a low-pass filtering effect (that is, toward the large scales). This fact has to be kept in mind and will be recalled when needed. Despite this limitation, the analysis of the obtained datasets provides valuable information on the characteristics of the eddy structures and their scaling and will be detailed here.

In this section, vortex characteristics and their Reynolds-number dependence are studied by computing probability density functions of different quantities. All these distributions are computed as follows. Let g be the quantity under study, N_{tot} the

total number of samples of g, and $N(g)$ the number of samples of g with a value between g and $g + \Delta g$, the probability density function pdf(g) of g is computed by

$$\mathrm{pdf}(g) = \frac{1}{\Delta g}\frac{N(g)}{N_{tot}}. \tag{5.1}$$

By using this definition, the integral of the function pdf(g) over the interval of known values of the quantity g is equal to 1. Thus, in the present study, the value of the probability density function of the quantities of interest (the vortex radius, vorticity, etc.) depends on the chosen scaling (e.g. wall-units or Kolmogorov scales). Moreover, the bin value Δg is taken to be 1/8 of the root mean square of g. Thus, the bin value is not necessarily the same for the same sets of data in different representations.

5.1.1. *Vortex location with respect to the wall*

Figure 15 shows the probability density functions pdf(y_0^+) and pdf(y_0/δ) of the wall-normal location of extracted vortices at both Reynolds numbers. Spanwise homogeneity has been checked and is shown for $Re_\theta = 7800$ in figure 15(*a*) only (symbols). As expected, the number of counter-clockwise rotating vortices is equal to that of clockwise rotating ones. For both Reynolds numbers, it appears that the near-wall region $y^+ < 150$ is more densely populated than the log layer, where the number of extracted vortices decreases slowly with wall distance. These results are in agreement with those obtained with the swirling strength itself (figure 7*a*) and with those of Carlier & Stanislas (2005). They also agree with the trends exhibited by the vortex population densities computed by Wu & Christensen (2006) from measurements obtained both in a turbulent boundary layer and a channel flow at different Reynolds numbers. When scaled in wall units, the density of the prograde spanwise vortices (e.g. vorticity of the same sign as the mean spanwise vorticity) estimated by these authors is decreasing with both the wall-normal distance and the Reynolds number. When plotted as a function of y/δ (figure 15*b*), distributions of the wall-normal locations of vortices collapse well, suggesting a Reynolds-number independence of the number of eddies in the log-layer in this representation.

5.1.2. *Vortex radius distribution*

The vortex validation method employed in the present study enables quantitative study of the radius of the identified vortices. Figure 16 shows probability density functions of the radius r_0^+ as a function of the wall-normal distance for the two Reynolds numbers. These statistics were computed by taking into account eddies contained in layers of 20 wall-units in height to improve the statistical convergence. At both Reynolds numbers, very near the wall, the width of the distribution as well as the peak value increase slightly with wall-normal distance and then stabilize for $y^+ > 150$. This behaviour is different from that observed by Tanahashi *et al.* (2004) in a channel DNS. These authors agree with the present behaviour for $y^+ > 150$, but they observe a slight increase of the radius when approaching the wall. In the present analysis, the largest radius of the detected vortices does not exceed 60 wall units.

These probability density functions, for the two Reynolds numbers, are superimposed in figure 17. The p.d.f. obtained by Carlier & Stanislas (2005) on the whole BL at $Re_\theta = 7500$ is also plotted for comparison. Although the number of samples was much smaller in that experiment, the p.d.f. agrees fairly well with the present results at $Re_\theta = 7800$ (taking into account the uncertainty on the friction velocity which is about 4% in Carlier & Stanislas 2005). The present data show that the radius distribution depends weakly on the wall-normal location throughout the

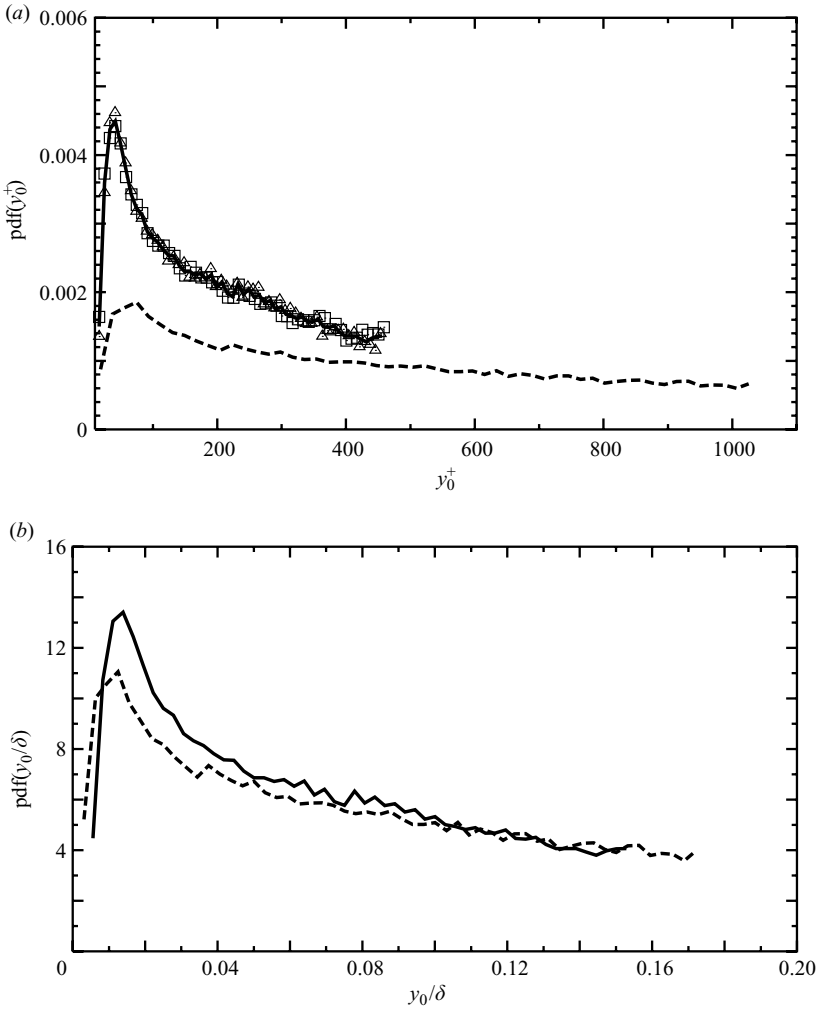

FIGURE 15. Probability density function of the wall-normal location of extracted vortices, (*a*) in wall unit and (*b*) normalized by the boundary-layer thickness δ, at (solid line) $Re_\theta = 7800$ and (dashed line) $Re_\theta = 15\,000$. (In *a*: □, counter-clockwise rotating vortices; △, clockwise rotating vortices, at $Re_\theta = 7800$).

log layer. The shape does not change much with the Reynolds number, but a shift of the mean value is clearly visible.

This is confirmed by figure 18 which gives the mean radius, in wall units, as a function of the wall distance. Here again, the data for the two Reynolds numbers are given, together with the results of Carlier & Stanislas (2005) for comparison. These correspond to measurements in a transverse plane inclined at 45° upstream, for four values of the Reynolds number, and to measurements in the (x, y)-plane at $Re_\theta = 7500$. The present results at $Re_\theta = 7800$ in the (x, z)-plane agree fairly well with those of Carlier & Stanislas (2005) in the (x, z)-plane at $Re_\theta = 7500$. It must be noted that the recording conditions of these two sets are fairly comparable (pixel size, interrogation window size and spatial resolution are very similar). Comparatively, the results of Carlier & Stanislas (2005) in the upstream tilted plane were obtained

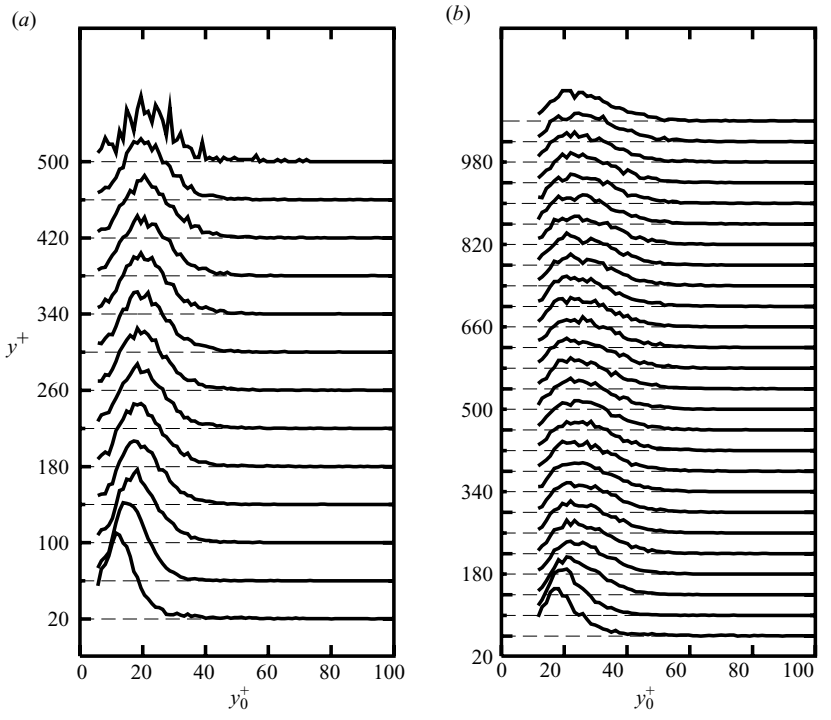

FIGURE 16. Probability density functions of the radius r_0^+ of the extracted vortices obtained at various height at (*a*) $Re_\theta = 7800$ and (*b*) $Re_\theta = 15\,000$.

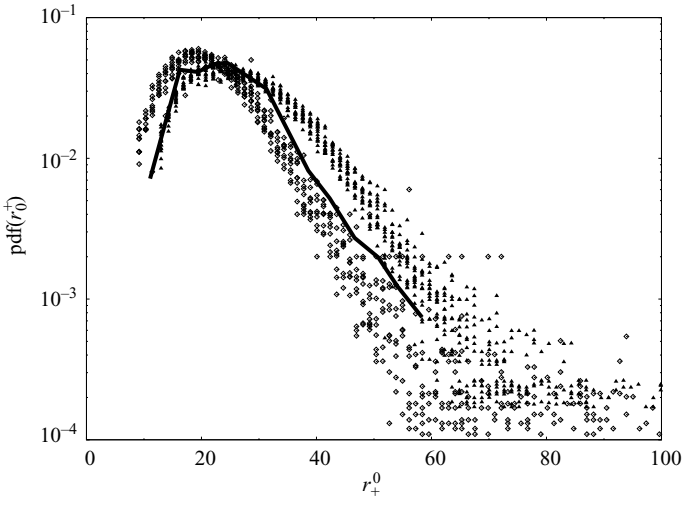

FIGURE 17. Probability density functions of the radius r_0^+ of the extracted vortices obtained in the logarithmic layer in wall unit scaling at $Re_\theta = 7800$ (◇) and $Re_\theta = 15\,000$ (▲); Carlier & Stanislas (2005) ($\boldsymbol{e}_x$, $\boldsymbol{e}_y$) plane and $Re_\theta = 7500$ (solid line).

with a comparable spatial resolution of 5 wu (the field of view was decreased when increasing the Reynolds number), but with an older PULNIX TM9701 camera which has bigger pixels (about twice as big, giving more peak locking) and is more noisy (8 bits instead of 16 for the grey-level coding). They are coherent between them,

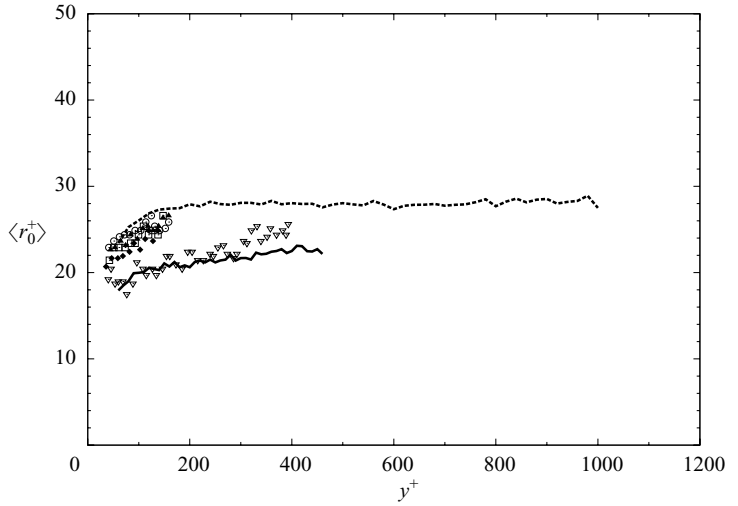

FIGURE 18. Wall-normal evolution of the mean radius of the extracted vortices obtained in the logarithmic layer scaled in wall unit. Present: (solid line) $Re_\theta = 7800$; (dashed line) $Re_\theta = 15\,000$. Carlier & Stanislas (2005): ∇, $(\boldsymbol{e}_x, \boldsymbol{e}_y)$ plane and $Re_\theta = 7500$; $\blacklozenge$, $(\boldsymbol{e}_z, \boldsymbol{e}_u)$ plane and $Re_\theta = 7500$; $\square$, $(\boldsymbol{e}_z, \boldsymbol{e}_u)$ plane and $Re_\theta = 10\,500$; $\blacktriangle$, $(\boldsymbol{e}_z, \boldsymbol{e}_u)$, plane and $Re_\theta = 13\,500$; $\bigcirc$, $(\boldsymbol{e}_z, \boldsymbol{e}_u)$ plane and $Re_\theta = 19\,000$.

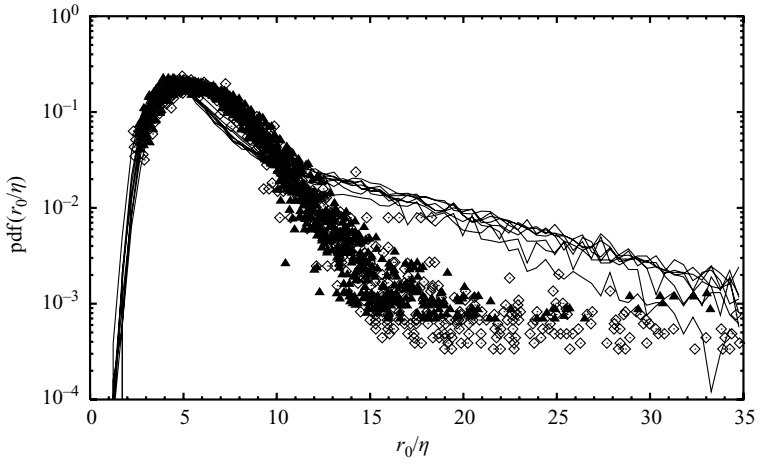

FIGURE 19. Probability density functions of the radius r_0 of the extracted vortices obtained in the logarithmic layer scaled with the local Kolmogorov scale $\eta(y)$ at $Re_\theta = 7800$ ($\diamond$) and $Re_\theta = 15\,000$ ($\blacktriangle$); solid lines, DNS of channel flow at $Re_\tau = 1270$ (Kang *et al.* 2005).

showing a relative independence with respect to the Reynolds number, but they are slightly above the preceding results, indicating that, probably, some of the smallest eddies have been missed, shifting the mean value slightly upward. In the present data, a shift upward is also clearly observed at $Re_\theta = 15\,000$. It is attributed to the lack of spatial resolution at this Reynolds number (as mentioned in § 2, the spatial resolution increases from 5 to 10 wu), which leads to missing also some of the smallest vortices.

In figure 19, the p.d.f. of r_0 is presented scaled with the Kolomogorov length scale $\eta(y)$ for both Reynolds numbers. In this figure, each vortex radius is scaled with $\eta(y)$

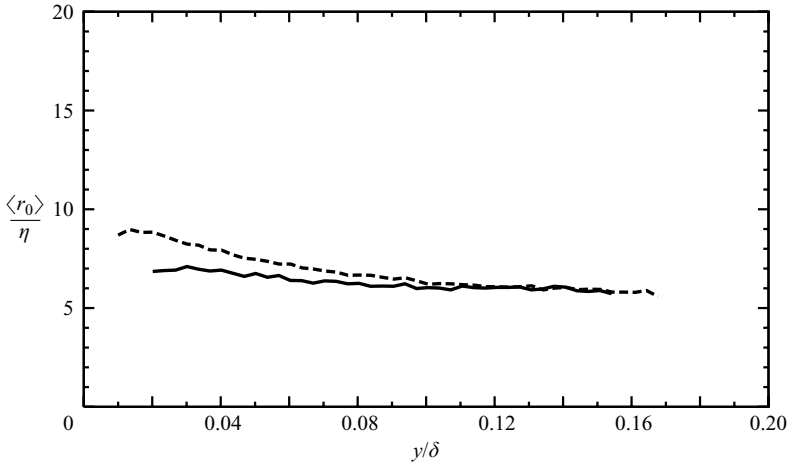

FIGURE 20. Wall-normal evolution of the mean radius of the extracted vortices obtained in the logarithmic layer scaled with the local Kolmogorov scale $\eta(y)$. (solid line) $Re_\theta = 7800$; (dashed line) $Re_\theta = 15\,000$.

at the ordinate of its centre before the p.d.f. is computed. Obviously, all the probability density functions collapse well, supporting the scaling already found by Tanahashi *et al.* (2004); Kang *et al.* (2005) and Das *et al.* (2006) in their DNS of channel flows. The fact that part of the smallest eddies are missed at the highest Reynolds number does not seem to affect the result, supporting strongly the universality of the representation (if they were captured, they would probably fall on the same curve). In this figure, these probability density functions obtained from experimental data are also compared to those obtained by Kang *et al.* (2005) in their DNS of a channel flow at a Reynolds number $Re_\tau = 1270$ (which can be compared to $\delta^+ = 2680$ and 4941 here). All the radius distributions are found to correspond well when the considered radius remains below $r_0/\eta < 12$. Above this value, some discrepancies appear between the experimental and the numerical results. This may be attributed to the experimental investigations being limited to one plane normal to both the wall and the mean flow (more or less streamwise vortices), while in the DNS, the above mentioned authors took into account all the vortices detected in the flow. Thus, the class of vortices corresponding to the larger scales is probably not exactly the same in both studies. It is important to note at this stage that the left part of the curves of figure 19 collapse well between experiments and DNS, and evidence vortices down to the Kolmogorov scale (although these are not fully captured by PIV).

Figure 20 gives the mean value of r_0 scaled by $\eta(y)$ and as a function of y/δ. This figure confirms the Reynolds-number independence in this representation. As discussed above, the small difference between the values obtained when approaching the wall at the two Reynolds numbers should be attributed to the difference in spatial resolution between the two experiments. The mean radius value obtained at $Re_\theta = 15\,000$ is somewhat overestimated, as the smaller scales tend to be discarded by the coarser spatial resolution in wall units. When considering the results obtained for the lowest Reynolds number, the value of the mean radius is almost constant and corresponds well to the value found by Kang *et al.* (2005) and Tanahashi *et al.* (2004) who evaluated the most expected diameter to be of 10–12 η in the log region. The slight increase toward the wall observed here at the highest Reynolds number is

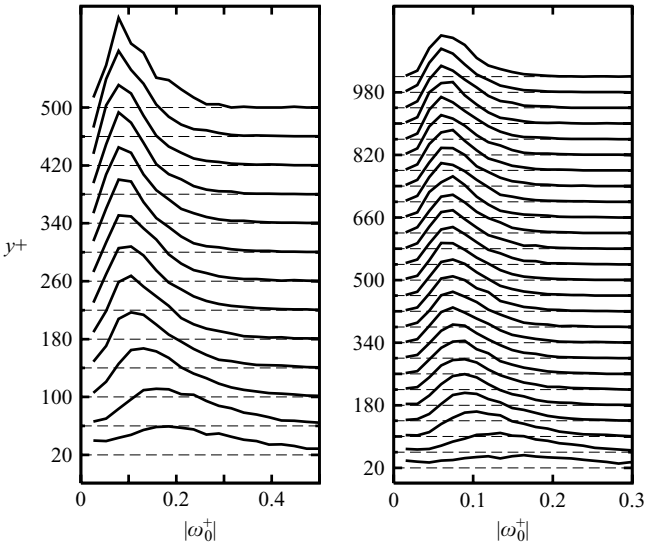

FIGURE 21. Probability density functions of the vorticity ω_0^+ of the extracted vortices obtained at various height at (*a*) $Re_\theta = 7800$ and (*b*) $Re_\theta = 15\,000$.

analogous to the finding of these authors. The above discussion leads to the hypothesis that the DNS of Tanahashi *et al.* (2004) was, maybe, slightly under-resolved near the wall.

The present results are in good agreement with those from the linear estimate of a swirling event in § 4.3 and reveal that the LSE slightly overestimates the mean radius of the individual vortices.

5.1.3. *Vorticity distribution of the eddies*

The same analysis as the one performed on the radius can be conducted on the vorticity deduced from Γ_0 in the model fit of (4.4). This is done here for both Reynolds numbers.

Probability density functions of the vorticity ω_0^+ obtained at various wall distances across the boundary layer are presented in figures 21(*a*) and 21(*b*). At both Reynolds numbers, the width of the distribution of this quantity, as well as the most probable value, decrease significantly with the wall-normal location and tend to saturate for $y^+ > 150$. This seems to indicate that, contrary to the near-wall region, the logarithmic layer is populated by a specific class of vortices that presents a limited range of vorticity fluctuation. The Reynolds-number effect in this representation (not shown) is comparable to that observed on r_0^+ and leads to the same conclusions.

Figure 22 presents the above probability density functions scaled by the local Kolmogorov time scale $\tau(y) = (\nu/\epsilon)^{1/2}$. This scaling leads also to the collapse of the probability density functions, bringing again strong support to the fact that the vortex characteristics can be normalized by dissipative scales (Tanahashi *et al.* 2004; Kang *et al.* 2005; Das *et al.* 2006).

The wall-normal evolution of the mean vorticity corresponding to the probability density functions in figures 22 is plotted in figure 23. This figure confirms the Reynolds-number independence of the vorticity when scaled by $\tau(y)$. The lower Reynolds number, which is the best resolved spatially, supports the idea of a constant value across the log layer in this scaling.

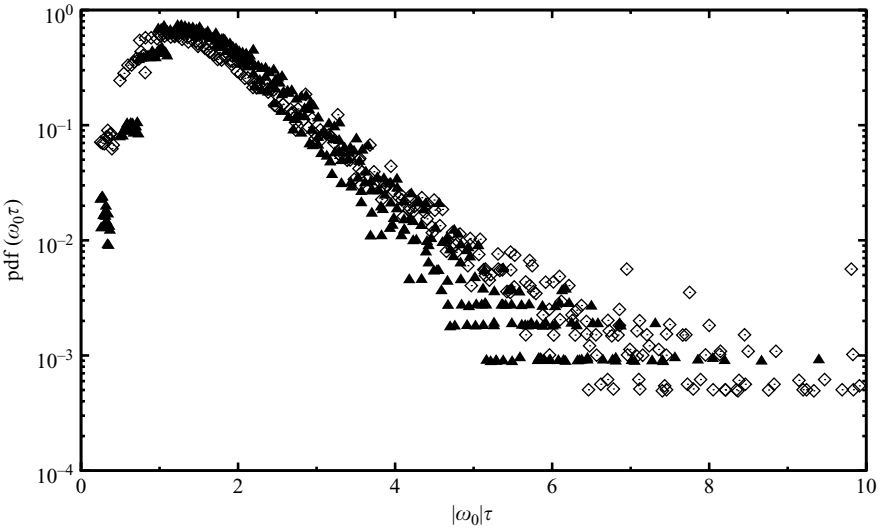

FIGURE 22. Probability density functions of the vorticity ω_0 of the extracted vortices obtained in the logarithmic layer normalized by the local Kolmogorov time scale $\tau(y)$ at $Re_\theta = 7800$ ($\diamond$) and $Re_\theta = 15\,000$ ($\blacktriangle$).

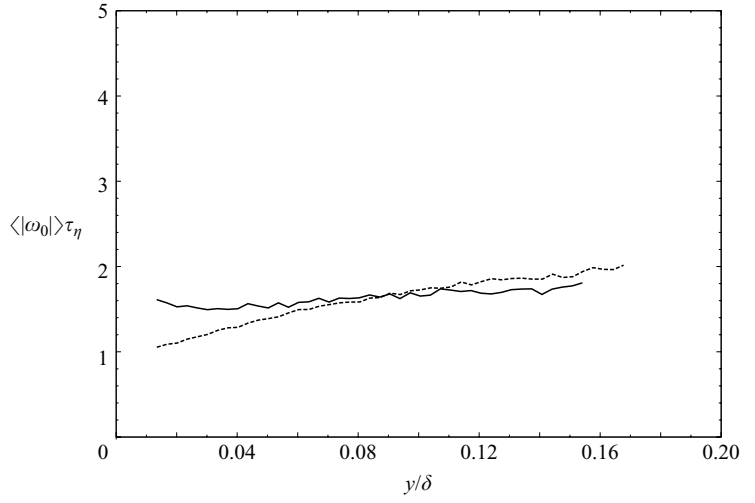

FIGURE 23. Wall-normal evolution of the mean vorticity of the extracted vortices obtained in the logarithmic layer normalized by the local Kolmogorov time scale $\tau(y)$, at (solid line) $Re_\theta = 7800$ and (dashed line) $Re_\theta = 15\,000$.

The eddy eduction method proposed in the present study enables the evaluation of characteristic parameters of the detected vortices, but also the computation of the maximal azimuthal velocity $u_{\theta max}$ via the analytical form of the model (equation (4.4)). Probability density functions of this quantity scaled by the Kolmogorov velocity scale $\upsilon = (\nu\epsilon)^{1/4}$ are presented and compared to the results of the DNS of Kang *et al.* (2005) in figure 24. As found by Tanahashi *et al.* (2004) and Kang *et al.* (2005) in their numerical studies, the distributions obtained throughout the log layer at both Reynolds numbers correspond well when normalized by the Kolmogorov scale. The

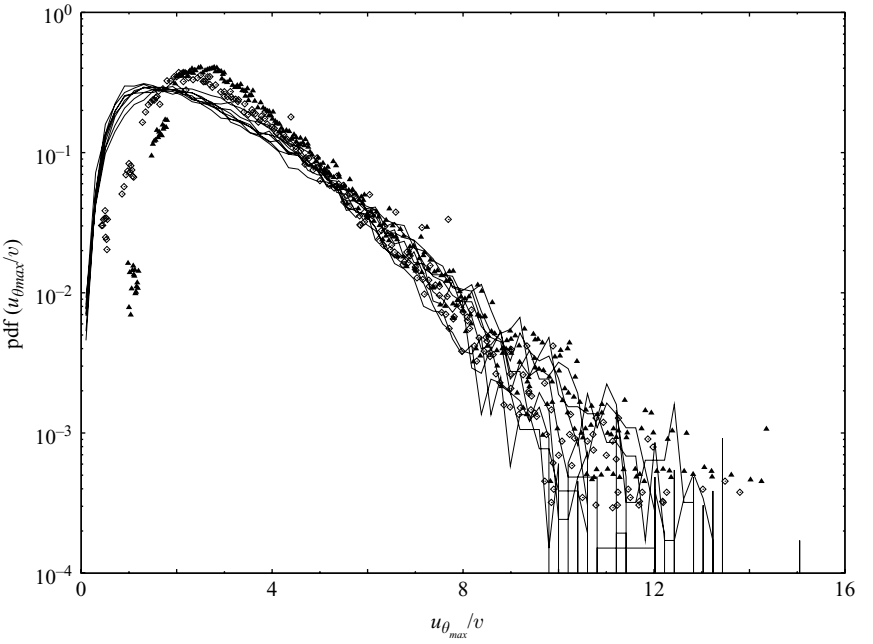

FIGURE 24. Probability density functions of the maximal azimuthal velocity $u_{\theta max}$ of the extracted vortices obtained in the logarithmic layer normalized by the Kolmogorov velocity scale $\upsilon(y)$ at $Re_\theta = 7800$ ($\diamond$) and $Re_\theta = 15\,000$ ($\blacktriangle$); solid lines, DNS of channel flow at $Re_\tau = 1270$ (Kang *et al.* 2005).

most expected value is between 2 and 2.5 υ which slightly overestimates the value found in the DNS studies of these authors. These differences should be attributed to the different detection techniques employed, as well as to the method used to evaluate $u_{\theta max}$. Probably, the lack of resolution of the smallest velocities by PIV, owing to its limited dynamical range also has some influence. This could explain the slight shift to the right of the peak between DNS and experiments. Nevertheless, distributions of the maximal azimuthal velocity, obtained both in the experiments and in the simulation, collapse reasonably well, confirming the Reynolds-number independence of the vortex characteristics when scaled with Kolmogorov scales.

5.2. *Conditional analysis*

Using the proposed vortex validation method, maps of the presence of vortices can be built. For each velocity map, a function is constructed by imposing the value of one in a circle of radius r_0 centred at the centre of each detected vortex and zero elsewhere. Clockwise and counter-clockwise rotating vortices are separated into two-groups. Then, two-point spatial correlations are computed in order to study the relationships between the two populations.

Figure 25 illustrates correlation maps between co-rotating vortices obtained at different wall-normal locations with a counter-clockwise rotating vortex at three reference points, including the LSE condition point of figure 11. Correlation maps show a single maximum corresponding to a self-correlation peak (which is normalized by the number of vortices at the given altitude) and no particular spatial organization owing to the interaction of co-rotating vortices. The correlation levels obtained in the surrounding of the main peak (of the order of 0.15) indicate that the probability of

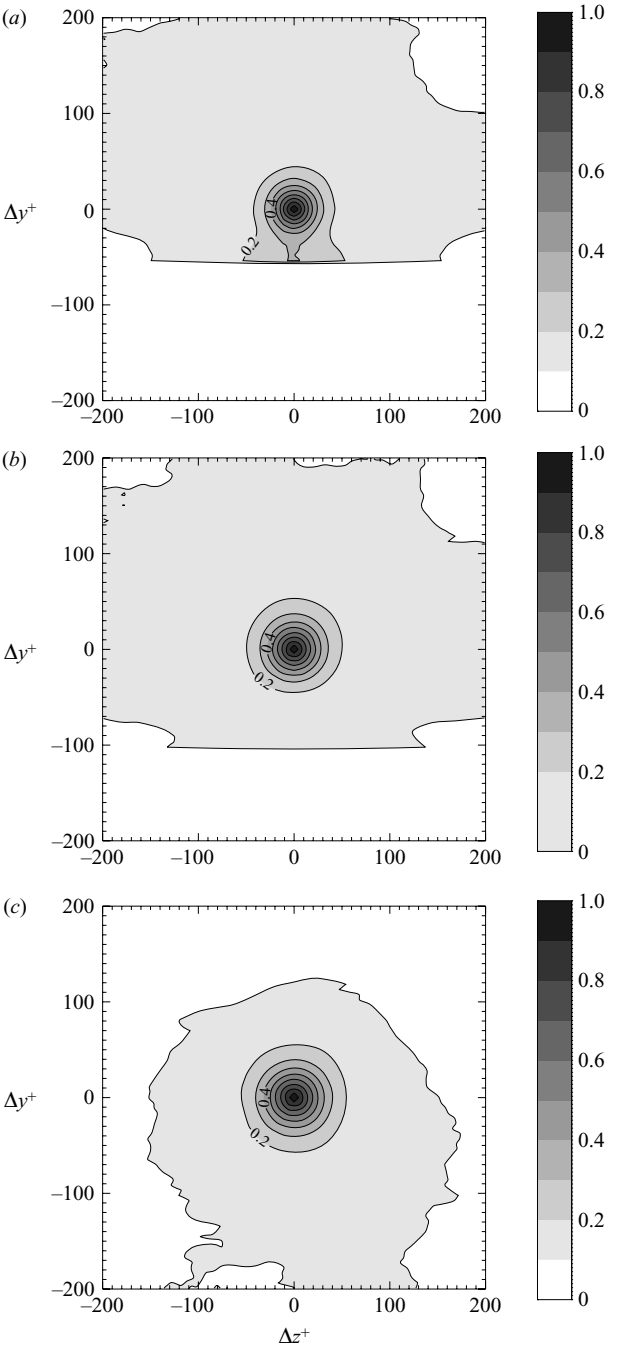

FIGURE 25. Correlation between co–rotating vortex for a counter-clockwise rotating vortices located at the reference point at (*a*) $y^+_{ref} = 50$, (*b*) $y^+_{ref} = 100$ and (*c*) $y^+_{ref} = 300$; contour increment of 0.1 from 0 to 1; $Re_\theta = 7800$.

having a vortex of the same sign in the neighbourhood of a given vortex is relatively low, but not zero, and uniformly distributed. To put an order of magnitude, at $Re_\theta =$ 7800, about 80 000 vortices have been detected in 2940 maps. This gives about

27 vortices in each field of 750×492 wu. With the hypothesis that these vortices are more or less evenly distributed, this gives about seven vortices in the field of figure 25(*a*). That is about three vortices of the same sign. Having one vortex at the fixed point, there are on average two vortices of the same sign around it in each instantaneous field building figure 25(*a*). The level of 0.15, as it is uniformly distributed, evidence this probability.

Figure 26 shows correlation functions between counter-rotating vortices obtained for a counter-clockwise rotating vortex at the reference point. For $y^+_{ref} = 50$ (figure 26*a*), counter-rotating vortices are more likely to be found at distances between 50 and 150 wall units from the fixed point. This can be viewed as the statistical imprint of the interaction of counter–rotating vortices via mechanisms of generation of secondary vortices (Zhou *et al.* 1999) or interaction between hairpin vortices within a hairpin packet (Tomkins & Adrian 2003) or the evidence of symmetrical hairpin structures. The maximum of correlation is located on the right-hand side of the reference point, at a distance of 75 wall units. This corresponds well to the picture of a quasi-symmetric hairpin-shaped vortex. However, the low level of correlation (less than 11 %) reveals that the probability of the existence of a two-legged hairpin structure remains weak. At $y^+_{ref} = 100$, the peak of correlation on the right-hand side is still present and nearly of the same amplitude (<11 %) as for $y^+_{ref} = 50$. A second peak is found below the reference point, on its left-hand side and may be attributed to the interaction with secondary vortices. At $y^+_{ref} = 300$, correlation levels remain higher on the right-hand side of the reference point, but just 2 % above the background level. Correlation maxima are weaker than in the near-wall region (<8%). Thus, in the logarithmic layer, the most probable vortical structure corresponds to a leg of a strongly asymmetrical hairpin structure, with a weak probability of finding a counter-rotating vortex in its neighbourhood.

Inspection of correlation maps obtained with a clockwise-rotating vortex located at the reference point shows similar results, but symmetrical with respect to the vertical axis, in agreement with the spanwise homogeneity of the flow.

6. Fluctuating vorticity budget

Having investigated thoroughly the characteristics of vortices in a turbulent flow, it is worth looking in detail at the equation for the mean square of the fluctuating vorticity field. This equation, which is given, for example, by Tennekes & Lumley (1972) is:

$$\begin{aligned} \overline{u}_j \frac{\partial}{\partial x_j}\left(\frac{1}{2}\overline{\omega_i'^2}\right) = {} & -\frac{1}{2}\frac{\partial}{\partial x_j}\left(\overline{\omega_i'\omega_i'u_j'}\right) - \overline{\omega_i'u_j'}\frac{\partial \overline{\omega}_i}{\partial x_j} + \overline{\omega_i'\omega_j'}\overline{s}_{ij}, \\ & [1] \qquad [2] \qquad [3] \qquad [4], \\ & + \overline{\omega_i'\omega_j's_{ij}'} + \overline{\omega}_j\overline{\omega_i's_{ij}'} + \nu\frac{\partial^2}{\partial x_j^2}\left(\frac{1}{2}\overline{\omega_i'^2}\right) - \nu\overline{\left(\frac{\partial \omega_i'}{\partial x_j}\right)^2} \qquad (6.1) \\ & [5] \qquad [6] \qquad [7] \qquad [8] \end{aligned}$$

where [1] is the convection by the mean flow, [2] is a turbulent diffusion term, [3] is the production by the gradient of mean vorticity (analogous to the production term of the turbulent kinetic energy equation), [4] represents the stretching/shrinking of $\overline{\omega_i'^2}$ by the mean rate of strain, [5] is a term of production of $\overline{\omega_i'^2}$ by turbulent

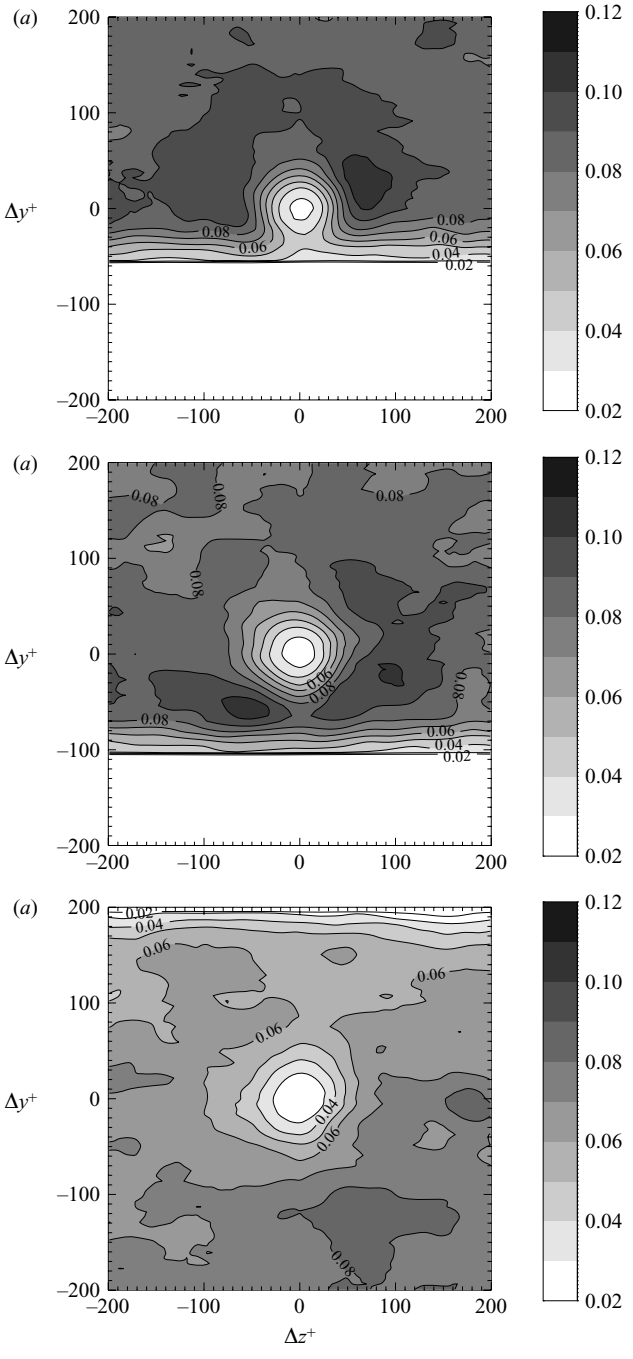

FIGURE 26. Correlation between counter-rotating vortex for a counter-clockwise rotating vortices located at the reference point at (*a*) $y^+_{ref} = 50$, (*b*) $y^+_{ref} = 100$ and (*c*) $y^+_{ref} = 300$; contour increment of 0.01 from 0.02 to 0.12; $Re_\theta = 7800$.

stretching, [6] has the specificity to appear both here and in the equation for $\overline{\omega_i}^2$ as a production term owing to stretching of fluctuating vorticity by strain rate fluctuations, [7] is viscous diffusion and, finally, [8] is the dissipation of $\overline{\omega_i'^2}$.

In their discussion (pp. 84–92), Tennekes & Lumley (1972) make an interesting analysis of the order of magnitude of the different terms of this equation in the case of a high-Reynolds-number 'two-dimensional mean flow' (that is $\overline{u}_3 = 0$, $\overline{\omega}_1 = \overline{\omega}_2 = 0$, $\partial/\partial x_3 = 0$ and $\partial/\partial x_1 \ll \partial/\partial x_2$). They come to the following estimation of the different terms:

$$[1] \quad \overline{u}_j \frac{\partial}{\partial x_j}\left(\frac{1}{2}\overline{\omega_i'^2}\right) \approx \frac{u^3}{\lambda^3}\frac{\lambda}{l},$$

$$[2] \quad \frac{1}{2}\frac{\partial}{\partial x_j}\left(\overline{\omega_i'\omega_i'u_j'}\right) \approx \frac{u^3}{\lambda^3}\frac{\lambda}{l},$$

$$[3] \quad \overline{\omega_i'u_j'}\frac{\partial \overline{\omega}_i}{\partial x_j} \approx \frac{u^3}{\lambda^3}\frac{\lambda^3}{l^3},$$

$$[4] \quad \overline{\omega_i'\omega_j'}\overline{s}_{ij} \approx \frac{u^3}{\lambda^3}\frac{\lambda^2}{l^2},$$

$$[5] \quad \overline{\omega_i'\omega_j's_{ij}'} \approx \frac{u^3}{\lambda^3}\cdot 1,$$

$$[6] \quad \overline{\omega}_j\overline{\omega_i's_{ij}'} \approx \frac{u^3}{\lambda^3}\frac{\lambda^3}{l^3},$$

$$[7] \quad \nu\frac{\partial^2}{\partial x_j^2}\left(\frac{1}{2}\overline{\omega_i'^2}\right) \approx \frac{u^3}{\lambda^3}\frac{\lambda^3}{l^3},$$

$$[8] \quad \overline{\nu\left(\frac{\partial \omega_i'}{\partial x_j}\right)^2} \approx \frac{u^3}{\lambda^3}\cdot 1$$

where u is the order of magnitude of the turbulent velocity fluctuations ($u \approx \sqrt{\frac{1}{3}\overline{u_i'^2}}$), l is the length scale of the energy-containing eddies (Taylor integral scale) and λ is the Taylor micro scale. This supposes some hypotheses on the order of magnitude of different single terms which are detailed by these authors; only two of them will be recalled here.

(i) The term $\overline{\omega_i'\omega_j'}$, which appears in [4], is estimated as $(u^2/\lambda^2)(\lambda/l)$ for $i \neq j$ (compared to $\overline{\omega_i'\omega_i'} \approx (u^2/\lambda^2)$), with the argument that the effect of the mean strain rate on the turbulent vorticity structure is weak, which can be represented by making it proportional to the time scale ratio $(\lambda/u)(u/l)$.

(ii) The correlation of velocity and vorticity fluctuations $\overline{\omega_i'u_j'}$ is estimated of order u^2/l, based on the fact that it is tightly linked to the gradient of Reynolds shear stress.

In fact, Tennekes & Lumley (1972) estimate the order of magnitude of all but the last term [8]. They observe that, at high Reynolds number, [5] dominates the other estimated terms and conclude that dissipation should balance term [5] and thus have the same order of magnitude. This leads to a fairly simple equation:

$$\overline{\omega_i'\omega_j's_{ij}'} = \overline{\nu\left(\frac{\partial \omega_i'}{\partial x_j}\right)^2}, \tag{6.2}$$

which is independent of the mean flow.

Based on dimensional similarity, this simple equation leads them to an estimation of the length scale characteristic of the fluctuating vorticity gradient, which they show to be proportional to the Kolmogorov length scale η. This conclusion is strongly supported by the results of § 5.

In fact, from the results obtained in the present contribution, set in the context of the above-mentioned literature, a few points can be emphasized concerning the physics of near-wall flows:

(i) The coherent vortices observed in the inner layer of the boundary layer scale with the Kolmogorov scales. This is deduced here from the analysis of PIV data and is in good agreement with the DNS results of Tanahashi *et al.* (2004), Kang *et al.* (2005) and Das *et al.* (2006),

(ii) In the log layer, these vortices seem, on average, to align preferably along the mean flow, at an angle of about 45° to the wall (which means that they somehow interact with the mean shear of flow),

(iii) There is a large variability around this mean picture of the vortex tubes in the log layer (see del Álamo *et al.* 2006),

(iv) The observed coherent vortices have a long lifetime and are seen to be transported by the mean flow in the near-wall region.

Based on these observations, it is of interest to revisit the analysis of Tennekes & Lumley (1972).

In order to give it more generality, let $\omega_i' \approx a\tau^{-1}$ be the order of magnitude of the fluctuating vorticity, with a a constant ($a \approx 1.6$ for the vortices detected in the present study) and τ the Kolmogorov time scale. Let then $b\eta$ be the length scale of the turbulent vortices with b a constant and η the Kolmogorov length scale ($b \approx 10$ in the present study if the mean vortex diameter is considered). Beside that, let V_j be the scale of the mean velocity component $\overline{u}_j$, and L_j the length scale in the evaluation of the gradient in the convection term. All the other terms are estimated as in Tennekes & Lumley (1972). On this basis, after dividing by $(a^2/\tau^2)(u/l)$, the different terms of (6.1) can be estimated as follows:

$$[1] \quad \overline{u}_j \frac{\partial}{\partial x_j}\left(\frac{1}{2}\overline{\omega_i'^2}\right) \approx \frac{V_j}{u}\frac{l}{L_j},$$

$$[2] \quad \frac{1}{2}\frac{\partial}{\partial x_j}\left(\overline{\omega_i'\omega_i'u_j'}\right) \approx 1,$$

$$[3] \quad \overline{\omega_i'u_j'}\frac{\partial \overline{\omega}_i}{\partial x_j} \approx \frac{1}{a}\left(\frac{ul}{\nu}\right)^{-1/2},$$

$$[4] \quad \overline{\omega_i'\omega_j'}\overline{s}_{ij} \approx 1,$$

$$[5] \quad \overline{\omega_i'\omega_j's_{ij}'} \approx \frac{l}{\lambda} \approx \left(\frac{ul}{\nu}\right)^{1/2},$$

$$[6] \quad \overline{\omega}_j\overline{\omega_i's_{ij}'} \approx \frac{1}{a},$$

$$[7] \quad \nu\frac{\partial^2}{\partial x_j^2}\left(\frac{1}{2}\overline{\omega_i'^2}\right) \approx \left(\frac{ul}{\nu}\right)^{-1},$$

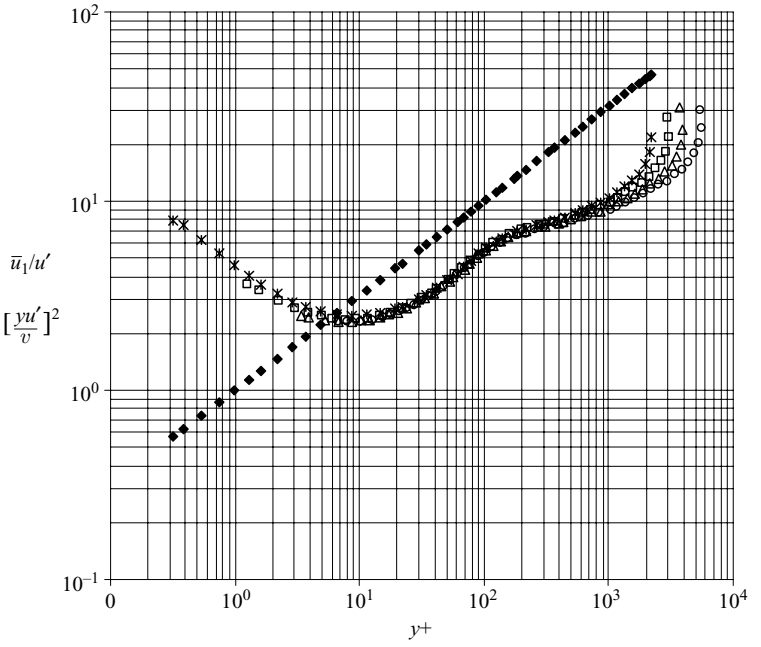

FIGURE 27. Ratio of the mean $\overline{u}_1$ and turbulent $u' = (\overline{u_1'^2})^{1/2}$ velocity scales as a function of y^+. $Re_\theta = 8200$ (∗); $Re_\theta = 11\,500$ (□); $Re_\theta = 14\,500$ (△); $Re_\theta = 20\,800$ (○); $(yu'/\nu)^{1/2}$ (◆); $u'/(yu'/\nu)^{1/2}$ (▲).

$$[8] \qquad \nu\overline{\left(\frac{\partial \omega_i'}{\partial x_j}\right)^2} \approx \frac{1}{a^2 b^2}\left(\frac{ul}{\nu}\right)^{1/2},$$

where u and l are the energy containing eddies scales, as previously defined.

A first remark is that, as a and b are of order 1 or more, it is the turbulent stretching term [5] which is the kernel of this equation at any scale. It is the only term which is just a Reynolds number at a positive power.

Taking in a first step $a = b = 1$ (that is looking at the Kolmogorov scale), $ul/\nu \gg 1$ and $V_j \approx u$ (as was done by Tennekes & Lumley 1972), we come to the same conclusion as these authors: the turbulent stretching [5] is balanced by viscous dissipation [8] and these two terms dominate all the others. This result obviously contradicts the observation that the vortices more or less align streamwise in the log layer.

To push the analysis to more detail, we must look first at the convection term [1] which, as the turbulent stretching term [5], does not involve the coefficients a and b in its order of magnitude (thus it has the same importance at all vortex scales). For this term to be significant, we should have at least $(V_j/u)(l/L_j) \approx (ul/\nu)^{1/2}$. Such a comparison can easily be performed using the present hot-wire measurements. As the main convective term corresponds to $j = 1$, (l/L_1) should be much smaller than 1, based on the standard boundary-layer hypothesis. We must then check the order of magnitude of (V_1/u). Figure 27 gives, for the four Reynolds numbers under study, $\overline{u}_1/\sqrt{\overline{u_1'^2}}$ as a function of y^+. On the same graph is plotted $(y\sqrt{\overline{u_1'^2}}/\nu)^{1/2}$. As can be seen, they are of comparable order of magnitude in the whole boundary-layer thickness, which means that, thanks to l/L_1, the convection term [1] can be neglected

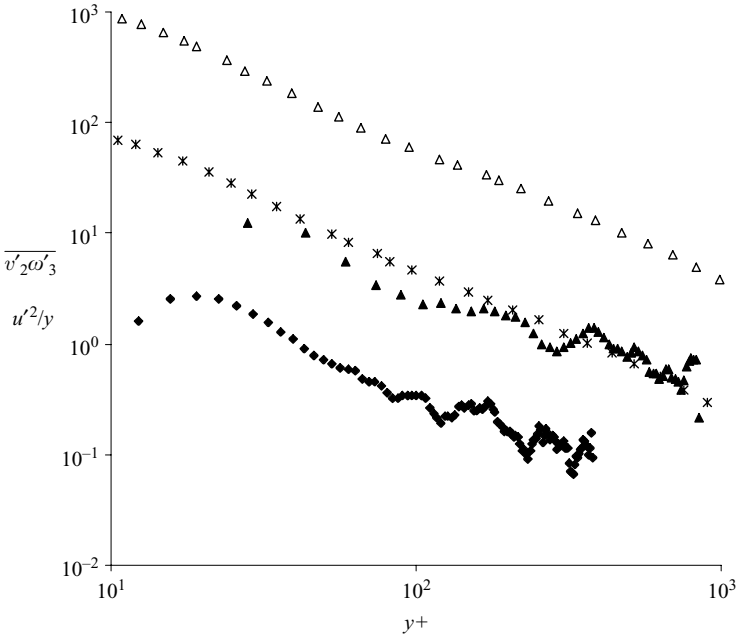

FIGURE 28. Correlation of the fluctuating velocity and vorticity components $\overline{v'_2\omega'_3}$ at $Re_\theta = 7800$ (◆) and $Re_\theta = 15\,000$ (▲) as a function of y^+ compared to u'^2/y at $Re_\theta = 8200$ (∗) and $Re_\theta = 14\,500$ (△).

with respect to term [5] in the inner region at least. Also note on this graph that $(y\sqrt{\overline{u_1'^2}}/\nu)^{1/2}$ becomes of order 10 only above y^+ of the order of 20 to 30. In the viscous sublayer, it goes to order 1 and terms [2] and [6] at least should be looked at.

The next terms to be estimated are those involving the interaction of the turbulent vorticity field with the mean flow velocity gradients. The first term including such a gradient is term [3]. This has been estimated here of order $au\tau^{-1}(u/l^2)$, leading to being negligible. The scaling of the mean vorticity gradient is difficult to question as it is merely a second derivative of the mean velocity. Besides, apart from the contributions of Klewicki (1989) and Priyadarshane *et al.* (2007), little is known on the velocity–vorticity correlation. To allow term [3] to be comparable to term [5], the order of magnitude of the velocity–vorticity correlation should be:

$$\overline{u'_j\omega'_i} \approx a\frac{u^2}{l}\left(\frac{u\lambda}{\nu}\right)^3. \tag{6.3}$$

This is much larger than the estimation of Tennekes & Lumley (1972) of u^2/l.

As the main mean vorticity component in a boundary layer is $\overline{\omega}_3$, which varies mostly along x_2, the main component of the above correlation tensor should be $\overline{u'_2\omega'_3}$. This correlation can be assessed from streamwise/wall normal (x, y) PIV data. This was performed here from the PIV data recorded by Kähler *et al.* (2000) which are stored in the WALLTURB database (wallturb.univ-lille1.fr). Figure 28 shows the plot of this quantity as a function of y^+ for the two Reynolds numbers available, together with u^2/y. As can be seen, in the whole range of investigation, the velocity–vorticity correlation is one to two orders of magnitude smaller than u^2/y, which means that the above condition cannot be fulfilled. The corresponding term [3] can thus be

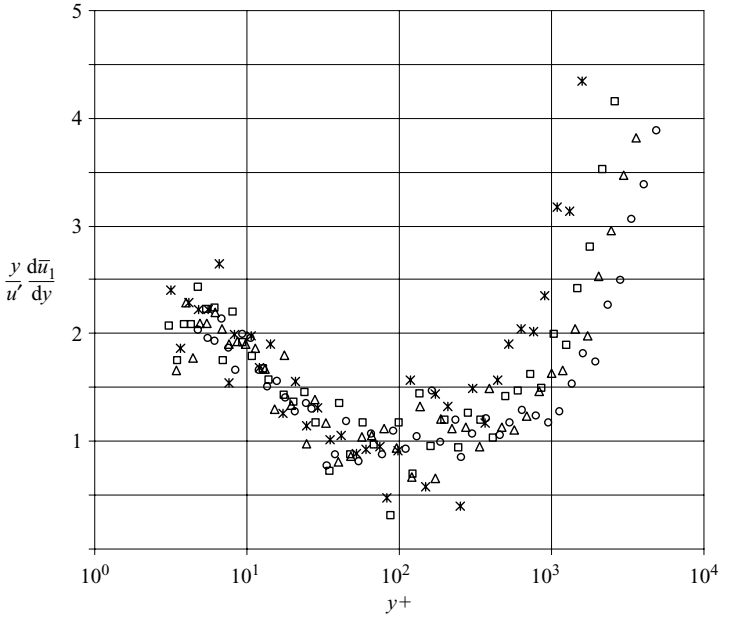

FIGURE 29. Mean velocity gradient $d\overline{u}_1/dy$ scaled with y and u' as a function of y^+. $Re_\theta = 8200$ (∗); $Re_\theta = 11\,500$ (□); $Re_\theta = 14\,500$ (△); $Re_\theta = 20\,800$ (○).

considered as negligible. The values provided by Klewicki (1989) and Priyadarshane *et al.* (2007) from multiple hot-wire measurements give a higher estimation of $\overline{u_2'\omega_3'}$, but which would lead it at best to be of order u^2/y.

The second (and last) term to look at in relation to mean velocity gradients is term [4], which involves the mean strain rate tensor. Again, the estimation of $\overline{s}_{ij} \approx u/l$ is difficult to question. In a boundary layer, the main component of the mean shear stress tensor is $\overline{s}_{12}$. Figure 29 shows $(d\overline{u}_1/dy)(y/u)$ as a function of the wall distance y^+. It is clear that this parameter is of order 1 in the whole boundary layer. Consequently, we must look at the order of magnitude of $\overline{\omega_i'\omega_j'}$. For term [4] to be comparable to term [5], we should have:

$$\overline{\omega_i'\omega_j'} \approx \frac{u^2}{\lambda^2}\frac{u\lambda}{\nu} \approx \frac{u^2}{\eta^2}. \tag{6.4}$$

This can be compared to the estimation of Tennekes & Lumley (1972) which is u^2/λ^2 and to the order of magnitude of $\overline{\omega_i'\omega_i'}$ which is estimated here as υ^2/η^2.

The question whether ω_1' and ω_2' are well correlated is difficult to answer quantitatively from the existing experiments, which do not give access to this quantity (a specific dual-plane PIV experiment should be performed for that purpose). Nevertheless, all the data available in the log layer show many vortices scaling on η inclined more or less at 45° downstream. This is a good indication of such a correlation. The Reynolds number $u\lambda/\nu$ being not so large, we can expect this statement to be true in the whole inner layer, whatever the size of the vortex is. Another strong argument supporting the effective action of term [4] is given in figure 30. This figure gives the mean convection velocity of the vortices as a function of wall distance for the two Reynolds numbers (7800 and 15 000) and compared with the

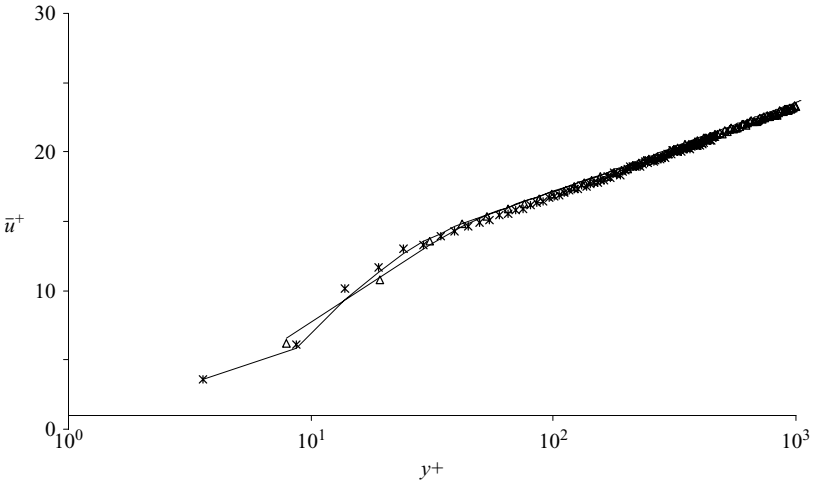

FIGURE 30. Mean streamwise convection velocity $\overline{u}_o^+$ of the vortices in the (y, z)-plane as a function of y^+, compared to the flow mean velocity $\overline{u}^+$. $Re_\theta = 7800$, convection velocity (∗), mean velocity (—); $Re_\theta = 15\,000$, convection velocity (△), mean velocity (- - -).

respective mean velocity of the flow. A logarithmic representation in wall units has been chosen to underline the region under study. A good portion of a real log layer is included at both Reynolds numbers. At $Re_\theta = 7800$, the limit of the viscous sublayer is reached. In both cases, data are available in the buffer layer. The figure clearly shows that the convection velocity of the vortices is very close to the mean flow velocity in both cases, and this in the whole field of investigation. It should be remembered here that this is the streamwise convection velocity of the legs of the hairpins. If the legs, at whatever wall distance they are cut, are convected at the local mean velocity, this means that on average, they are stretched by the mean shear. The corresponding term has thus to be kept in the budget and its order of magnitude as estimated in (6.4) is justified *de facto*.

The last term to consider is the dissipation term [8]. In the present scaling, the main difference with the Tennekes & Lumley (1972) analysis is the coefficient $1/a^2b^2$ in the estimation of this term. This coefficient is representative of the fact that dissipation depends strongly on the scale of the vortices (b^2). When considering vortices of the Kolmogorov size, $a = b = 1$ and this term is comparable to term [5]. Now, looking at the mean vortices in the present study, $a \approx 1.6$ and $b \approx 6$. This leads to $a^2b^2 \simeq 100$, which means that the dissipation of fluctuating vorticity is already negligible at one order of magnitude above the Kolmogorov scale. Vortices have to go down to the Kolmogorov scale to be killed by viscosity. We can thus expect the observed mean vortices to have a lifetime much longer than τ (which should be interpreted here more as a turnover time) and to be stretched on significant distances by the mean shear in the near-wall region.

As a consequence of the above analysis, equation (6.1) for the mean square vorticity fluctuation should be:

$$0 = \underset{[2]}{-\frac{1}{2}\frac{\partial}{\partial x_j}\left(\overline{\omega_i'\omega_i'u_j'}\right)} + \underset{[4]}{\overline{\omega_i'\omega_j'}\overline{s}_{ij}} + \underset{[5]}{\overline{\omega_i'\omega_j's_{ij}'}} + \underset{[6]}{\overline{\omega}_j\overline{\omega_i's_{ij}'}} - \underset{[8]}{\nu\overline{\left(\frac{\partial\omega_i'}{\partial x_j}\right)^2}} \tag{6.5}$$

in the viscous sublayer, and

$$0 = \underset{[4]}{\overline{\omega_1'\omega_2'}\bar{s}_{12}} + \underset{[5]}{\overline{\omega_i'\omega_j's_{ij}'}} - \underset{[8]}{\nu\overline{\left(\frac{\partial\omega_i'}{\partial x_j}\right)^2}} \tag{6.6}$$

in the buffer and log layers.

Equation (6.5) appears fairly complicated and is difficult to comment on further based on the present results, as they do not resolve the viscous sublayer. Equation (6.6) differs from that of Tennekes & Lumley (1972) only in term [4] and is fairly coherent with the observation from both experiments and DNS in the log layer: more or less distorted vortex tubes which size on Kolmogorov scales and which have relatively long lifetime travel along the wall and align more or less at 45° downstream (term [4]) but with a high variability (term [5]). As underlined by figure 5, significant energy dissipation occurs in the buffer and viscous sublayers. The similarity of the distribution of figures 5 and 15 supports the idea that part of this dissipation is done by the vortices themselves. The above analysis indicates that, in vortices, this dissipation occurs mostly at the Kolmogorov scale and that the vortices observed in the buffer and log regions, which are about 10 η on average, already dissipate very little. The dissipation term should nevertheless be kept in (6.6), as the p.d.f. of vortices clearly show that Kolmogorov scale vortices can be found in the whole region under study. The decrease of ϵ away from the wall could thus be linked to the decrease of the mean number of vortices and not to a change in their size distribution (cf. figures 5 and 15).

7. Discussion

Having recognized from the literature survey that vortices play an important role in near-wall turbulence, and a certain number of them preferably align more or less with the mean flow, the present contribution was focused on streamwise vortical structures existing in a turbulent boundary layer. The aim was to investigate the dynamics of these eddies in the buffer and log layers and to try to extract some useful scaling from the data. For that purpose, velocity fields acquired by stereoscopic PIV in the (y, z)-plane at Reynolds numbers $Re_\theta = 7800$ and 15 000 were analysed using different mathematical tools. In particular, a vortex extraction method has enabled us to determine quantitative characteristics of vortices cutting this plane. Also, given the spatial character of the available measurements, spatial organization and distribution of these vortices could be studied in detail with different mathematical tools.

The first point that comes out of this analysis is the difference in vortex characteristics and behaviour between the region above $y^+ \simeq 150$ (say above 100 to 200, that is in the log layer) and the region below this limit (say in the buffer layer, as the viscous sublayer is not resolved here). This result is coherent with the behaviour of the skewness and flatness factors of the streamwise velocity fluctuations displayed in § 3. These quantities reveal a strong change in the turbulence physics between $y^+ = 10$ and 150. The data presented here do not resolve the viscous sublayer, but they are in agreement with the upper limit of 150.

The second important result concerns the shape of these streamwise vortices. The predominance of hairpin-shaped structures as a main element of the turbulent boundary-layer structure has been already suggested by several authors (Head & Bandyopadhyay 1981; Perry & Chong 1982; Adrian *et al.* 2000*b*; Hutchins *et al.* 2005).

The vortex extraction technique used here, combined with the chosen measurement configuration, was expected to provide information on the leg parts of these coherent structures. As the detection scheme used is based only on a swirling event and as the information is available in only one plane at a time, we must bear in mind that some of the detected vortices can be isolated, with no direct relationships with wall-attached hairpin structures. However, some effective and quantitative conclusions can be drawn from the present results.

Investigation of the two-point spatial correlation tensor of the swirling strength, of the one- and two-point LSE, as well as the conditional analysis of the presence of vortices, reveal that the most probable form of streamwise vortices is strongly asymmetrical and probably resembles a cane or hook more than a hairpin. This conclusion was already supported by the results of Carlier & Stanislas (2005), who found about twice as many heads as legs of one sign in the log layer. Statistical evidence of counter-rotating vortices, which could be the footprint of more symmetrical structures is found only in the very near-wall region. Negative levels of $R_{\lambda_s\lambda_s}$ are of the order of 5 %, for $y^+ \leqslant 100$ and the probability of finding counter-rotating vortices is shown, in the conditional analysis, to be higher in the near-wall region. Moreover, the above correlation tensor turns out to be rather isotropic (e.g. in this region, negative correlation can be found in all the domain surrounding the reference point), indicating that no preferred organization exists. If the distance between the reference point and a negative extremum of correlation is in good agreement with the streak width found experimentally by Stanislas *et al.* (2005) (see also Lin 2006), the isotropic character of the correlation pattern is more favourable to the existence of asymmetrical vortices interacting with each other via:

(i) mechanisms of vortex generation, as proposed by Hanratty & Papavassiliou (1997), who supposed that new vortices are created by the interaction of older vortices with the wall;

(ii) secondary vortices generated by hairpin vortices present in hairpin packets as evidenced by Zhou *et al.* (1999);

(iii) mechanisms of vortex annihilation that imply mutual vorticity cancellation as suggested by Perry & Chong (1982);

(iv) turbulent dissipation.

The linear stochastic estimation, performed with one or two conditions, fully supports the above conclusion. If there is a coupling between nearby vortices, it should be through processes leaving no imprint in the LSE analysis. This least-squares analysis provides a clear image of a single vortex which, if positive (counterclockwise), is linked to a low-speed lifting region on its right and a high-speed sweeping region on its left. These side regions increase in size when going away from the wall, while the vortex stays nearly constant in size and intensity.

Conditional analysis conducted with the vortex validation method proposed by Carlier & Stanislas (2005) confirms that most vortices are present in an asymmetrical form (the probability of finding counter-rotating vortices remains below 11 % and is mostly located below $y^+ = 150$). Although a peak of probability corresponding to the classical picture of a two-legged hairpin vortex exists in the near-wall region, its level is only a few per cent above the background level. Thus, if two-legged hairpins exist, the most probable vortices are asymmetrical ones. Inspection of instantaneous velocity fields and maps of the position of the detected vortices (not shown) supports these conclusions.

The third point to emphasize is that, based on the quantitative data provided by the different approaches, some scaling information can be derived from the present

results. Evaluation of the radius of the detected streamwise vortices by correlation of swirling strength, linear stochastic estimation of a swirling event or by the fit of an Oseen vortex model are in good agreement. This gives some confidence in the results. The latter two methods reveal that the characteristic size of eddies first increases slightly with y in the near-wall region and then tends to become almost constant for $y^+ > 150$. This result is in good agreement with the previous study of Carlier & Stanislas (2005) in a similar configuration and also with the numerical studies of Tanahashi *et al.* (2004) and Kang *et al.* (2005). By using the evaluation of the Kolmogorov length $\eta(y)$, time $\tau(y)$ and velocity $\upsilon(y)$ scales from available hot-wire measurements, both the characteristic radius, vorticity and maximum azimuthal velocity of the detected vortices are found to scale with the local Kolmogorov scales throughout the logarithmic region. With this scaling, distributions of the radius and vorticity associated to the detected vortices are also found to be independent of the wall-normal location of the vortex position. The mean radius of the vortices is of the order of 6η (with a distribution between 1 and 30η). The mean vorticity is about $1.6\ \tau^{-1}$ (with a distribution between 0 an $10\ \tau^{-1}$). As shown by figures 17 and 24, the present results, based on the experimental investigation of boundary-layer flows at Reynolds numbers Re_θ up to 15 000, are fully consistent with those from the numerical study of Kang *et al.* (2005) performed in channel flows at Reynolds number Re_τ up to 1270. As will be seen later on, this result is important, as it emphasizes the importance of the Kolmogorov scales in wall turbulence.

In their contribution, Tomkins & Adrian (2003) studied the spanwise growth of hairpin structures by analysing the width of the conditionally extracted hairpin. In fact, this scale was based on a measure of the width of the low-speed regions at zero streamwise separation. They found that, on average, this scale evolves almost linearly with y, with a growth rate value of almost 1. Consequently, the mechanism of spanwise growth that they proposed predominantly affects the regions of constant longitudinal velocity rather than the vortical structures constituting the leg and head parts of the hairpin-shaped vortices themselves. It is in agreement with the growth of the regions of high and low streamwise velocity observed here with the one-point LSE (figure 11).

Study of the wall-normal distribution of the detected vortex number (figure 15*b*) shows that we can distinguish two regions. The near-wall region (e.g. for $y^+ \leqslant 150$) exhibits a large number of vortices (and a high level of dissipation, see figure 5), which decreases rapidly away from the wall. In the logarithmic region, the vortex density still decreases, but with a slower rate. It should be noted here that a plot in logarithmic scale of this quantity (not shown here) suggests that it may follow a power law as a function of y in the logarithmic region.

The evolution of the number of vortices obtained in the present study is in good agreement with previous studies on mechanisms of wall turbulence (Panton 1997) which showed that most of the vortices are produced in the near-wall region and then lift up away from the wall. From the present observations, a scenario for the life-cycle of vortices can be suggested: vortices are mostly generated in the near-wall region via various mechanisms involving spanwise instabilities, vortex–wall interaction (Panton 1997) or auto-generation from existing hairpin structures (Zhou *et al.* 1999). They then undergo strong stretching, owing to the important mean velocity gradient in the very near-wall region (see figure 29), which leads to a thinning of the vortex tubes and an increase of the dissipation process within the vortical structures. This mechanism finally ends with the death of part of the eddies. In this densely populated region, vortices may also be submitted to interaction with each other through pairing

mechanisms (between co-rotating vortices) or vorticity cancellation (between counter-rotating eddies). As a consequence, a large fraction (almost 50 %, see figure 15) of the created eddies disappears in the region between the wall and $y^+ = 100$. The 'surviving' vortices amalgamate in clusters (Tanahashi *et al.* 2004) that are stretched up, and in which processes of self- and mutual induction can lead to lift-up motion. Thus, vortices propagate throughout the logarithmic layer where velocity gradients become weaker. This scenario is consistent with the simplified wall–turbulence model proposed by Perry & Chong (1982) and Perry & Marusic (1995), except for the Λ-shaped vortices they use in their study. Nevertheless, the present results should help to design vortex distribution in models such as those cited above.

As mentioned earlier, Hutchins *et al.* (2005), via the analysis of the two-point spatial correlation of the longitudinal velocity component, came to the conclusion that two regimes, defined as attached or detached eddies, exist: near the wall, where events are still strongly influenced by it; or away from the wall where no-correlation exists with events at the wall. Looking at the correlation that exists here between vortical motion and regions of constant longitudinal velocity (figure 11), the results of Hutchins *et al.* (2005) corroborate the scenario proposed in the present paper, in which vortices present in the logarithmic region have limited influence from the wall.

Based on the above analysis and on the fact that the Kolmogorov scale is nearly constant very near to the wall and universal in wall units in the whole inner layer (figure 6 gives $\eta^+ \approx 2$ up to $y^+ \approx 30$), it is possible to revisit the well-known structure of this inner layer in the light of the Kolmogorov vortices.

(i) The viscous sublayer, which is commonly considered as 5 wu thick is thus about 2.5 Kolmogorov scales. Remembering from figure 17(*b*) that the radius of individual vortices goes down to η, this layer has a thickness of the order of the diameter of Kolmogorov vortices. If such vortices exist, they should be more or less parallel to the wall. They should strongly interact with the wall and dissipate. This is supported by the distribution of ϵ in figure 5. It is probable that, owing to this strong dissipation, these vortices have a short lifetime, of the order of their turnover time τ (of the order of 100 μs near the wall at $Re_\theta = 20\,800$).

(ii) The standard buffer layer, which is about 50 to 60 wu thick is about 25 to 30 Kolmogorov scales. In this region, vortices with a radius of the order of 10η (one order of magnitude bigger than in the viscous sublayer) should be more or less parallel to the wall. These are the wall-attached streamwise vortices put in evidence by many authors in this buffer layer (Panton 1997). Lin (2006) studied them in detail and showed that they are centred between 20 and 30 wu, parallel to the wall and with a spanwise angle with an r.m.s. value of the order of 15°. These vortices last much longer than the Kolmogorov ones as it was shown here that they dissipate very little intrinsically. They probably dissipate somehow by interaction with the wall. It should be noted here that $S(u)$ shows a minimum at 30 wu (15η) and $F(u)$ at 15 wu, which may be the imprint of these streamwise vortices. From such a picture, it appears that the whole viscous and buffer layers would be dominated by vortices in the range of 1 to 10η in radius, more or less parallel to the wall owing mostly to their respective size and wall distance. It should be emphasized here that this is a region of high turbulence intensity where the peak of vortex population is observed (figure 15). This is also the region where an instability mechanism, which is not yet fully agreed upon is supposed to generate these vortices.

(iii) Between this buffer layer, where most vortices are generated, and $y^+ \simeq 150$ (of the order of 100η), there is some freedom for vortices which are about 10η in radius to lift up and interact with each other. The vortex population in this region is still

high, but decreases rapidly owing to these interactions. Inclined vortices are observed, preferably downstream owing to term [4] of (6.7), but with a high variability owing to term [5].

(iv) The log layer which extends here above $y^+ \simeq 150$ and up to y^+ in the order of thousands ($\approx$1000 η too) at high enough Reynolds number, leaves much more freedom for the vortices to develop, but the experimental evidence is that the stretching generated both by the mean velocity gradient and by the turbulence leads them to stay on average at the limit of dissipation ($\approx 10\eta$). This is partly due to term [4] of (6.7), but also to term [5] which appears to grow in that region as shown by figure 27.

(v) The wake region is most probably a region where term [4] ceases progressively to have influence and where (6.7) returns to the original Tennekes & Lumley (1972) form.

As can be seen, it is possible to describe the whole boundary layer in terms of the behaviour of vortices scaling with Kolmogorov scales. The highest population of these vortices appears to be: located between 20 and 30 wu; nearly streamwise; and more or less parallel to the wall. This seems to indicate that they are generated there by some instability phenomena (not lower because the viscosity is too strong; not higher because the velocity gradient is too weak). If parts of these vortices move down to the wall, they should be strongly stretched by the high mean velocity gradient existing there (see figure 29) and bound to stay more or less parallel to the wall. They probably dissipate very quickly. On the contrary, the vortices that move away from the wall have much more freedom. They can lift up, change orientation and reorganize in the upper part of the buffer layer and then develop in the log region.

Of course, as a direct consequence of this analysis, comes the question of the wall friction. To discuss this point, recall the above estimation of the Kolmogorov length scale near the wall:

$$\frac{\eta u_\tau}{\nu} \approx 2. \tag{7.1}$$

In fact, this equation is usually looked at as a scaling of η with u_τ and ν: the standard wall scaling. In the light of the above discussion, it can now be interpreted as a scaling of u_τ with η and ν. If the Kolmogorov scale governs everything in the near-wall region, it should govern the wall friction.

Going back for a moment to the flat-plate laminar boundary layer, it has been known since Blasius that it scales with the external velocity U_e and the fluid viscosity ν. This viscosity is directly responsible for the friction at the wall and representative, at the level of the continuum, of the Brownian motion. In turbulent boundary layers, two scalings are classically used: the outer scaling based on U_e, u_τ and δ (the velocity deficit $U_e - U$ scales with u_τ and δ) and the inner scaling based on u_τ and ν. Specific scalings have also been proposed, for example by Graaf & Eaton (2000) for u'^2, but none of them has yet succeeded in representing the whole boundary-layer thickness with a single set of scaling parameters. If the Kolmogorov scales really determine the friction at the wall, and if they are more representative of the dissipation process than ϵ, they should replace ν and a scaling based on U_e and η should work near the wall. The fluid viscosity would become then a kind of secondary 'turbulence thermodynamic quantity', by contributing (with the dissipation rate) to fix the size η of the Kolmogorov scale.

Before looking at this hypothesis, it is worth looking at the integral scales. Figure 31 gives, for the four Reynolds number under study, the ratio η/y as a function of y^+ (which is considered here as a realistic estimator of ul/ν). On this figure is also plotted, as a solid line, the fit $0.8(y^+)^{-3/4}$ to these data which are universal in this

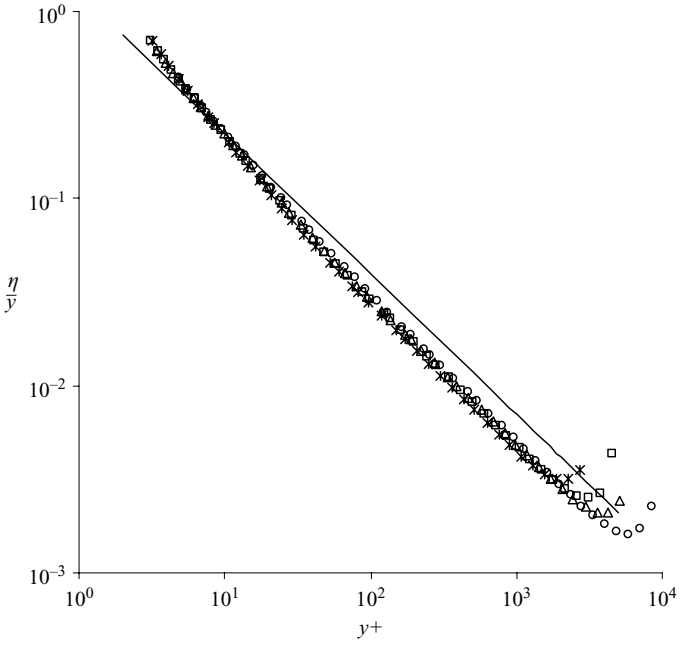

FIGURE 31. Kolmogorov length scale η compared to integral scale y as a function of y^+. $Re_\theta = 8200$ (*); $Re_\theta = 11\,500$ (□); $Re_\theta = 14\,500$ (△); $Re_\theta = 20\,800$ (○); $0.8(y^+)^{-3/4}$ (—).

representation. This fit comes from $\eta^+ = (\kappa y^+)^{1/4}$ which gives $\eta^+/y^+ = \kappa^{1/4}(y^+)^{-3/4}$ with $\kappa = 0.41$. This result shows that y is in fact a good estimator of the integral scales at a given wall distance (as $\eta/l \approx (ul/\nu)^{-3/4}$). This figure also shows that the ratio of integral to Kolmogorov scales is of order 1 very near the wall and that it decreases rapidly away from it. This supports the idea that, very near the wall, η should be the scale of reference as it is there both the integral and dissipative scale. Now, from what is known since Kolmogorov on turbulence, when the ratio of these two scales is large enough (high enough turbulent Reynolds number) the standard cascade process should take place and turbulence should scale on the energy-containing eddy scales, that is on something of the order of the boundary-layer thickness in the wake region. This is the difficulty encountered up to now to link the internal and external scales of the boundary layer. This scaling problem is illustrated here in a different way in figure 33. The ratio U/U_e is plotted as a function of y/η. A good universality is obtained near the wall, as good as with the standard wall scaling (see figure 5 of Carlier & Stanislas 2005), but not in the outer part of the BL. This result is of course of interest because one external parameter, the free-stream velocity U_e is used, establishing a link between the external and near-wall flows. Then, only the length scale can be expected to change from η near the wall to something representative of the integral scales away from it (for which δ is a good candidate).

Looking at figure 6, we can see that η is slowly growing away from the wall while, as shown in figure 32 which gives η/y as a function of y/δ in a log–log representation, the ratio of scales goes progressively to several orders of magnitude when y increases. It would thus be difficult to switch from η to δ continuously. As the similarity theory tells us that anything proportional to δ would work as well, it is proposed here to

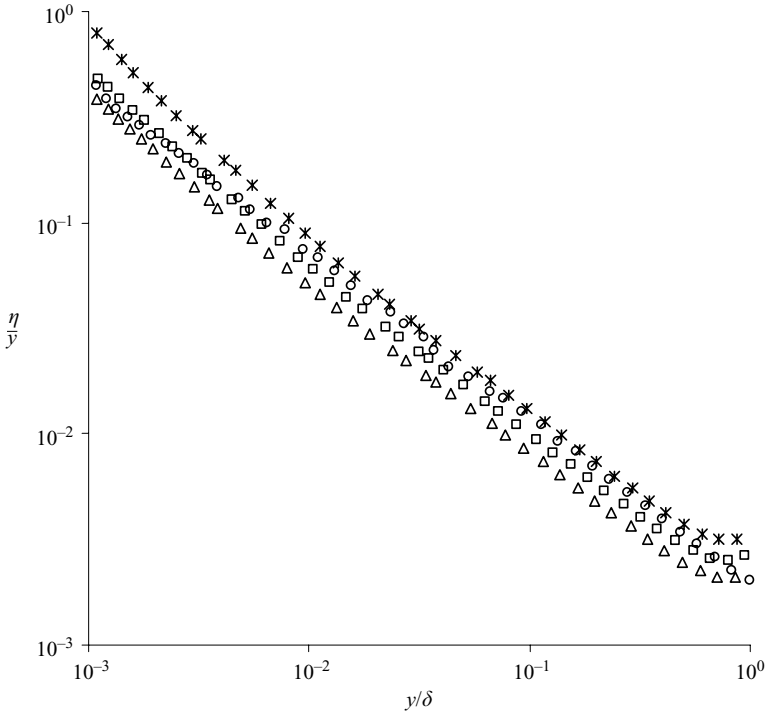

FIGURE 32. Kolmogorov length scale η compared to integral scale y as a function of y/δ. $Re_\theta = 8200$ (*); $Re_\theta = 11\,500$ (□); $Re_\theta = 14\,500$ (△); $Re_\theta = 20\,800$ (○).

define a new length scale $\eta*$ of the form:

$$\eta^* = \min\left(\eta, \frac{\delta}{A}\right). \tag{7.2}$$

This equation says that δ takes over as a scaling length when a ratio of A is reached between 'integral' and Kolmogorov scales. The above proposed parameter allows one to switch continuously the length scaling from $\eta(y)$ to δ in the corresponding regions of the flow, keeping U_e as the velocity scale in the whole boundary layer.

The choice of A is somehow connected with the extent of the turbulence spectrum. Different tests on the present data lead A to be of the order of 1000. This value is not very sensitive. Between 900 and 1100, relatively comparable results are obtained. The value $A = 1000$ is thus retained as it can be interpreted easily: the switch occurs when there are three orders of magnitude at least between δ and η. If Kolmogorov scale η is less than $\delta/1000$, it is far enough from the flow scales to be fully representative of the dissipation process only. If it is above this order of magnitude, it becomes a kind of mixed length scale which is not adequate for scaling the flow properly.

Figures 34 to 37 give, respectively, the mean velocity gradient, the mean velocity profile, the profiles of the three turbulent intensities and the profile of the Reynolds shear stress in the proposed scaling, for the four Reynolds numbers under study. Apart from the lowest Reynolds number, which shows a slightly different behaviour, probably owing to the low-Reynolds-number effect (and maybe partly to the difficulty of measuring with hot wires at low velocities), all these quantities show good universality in this representation (taking into account the crude approach used for the determination of η from the hot-wire data). The agreement is apparently not

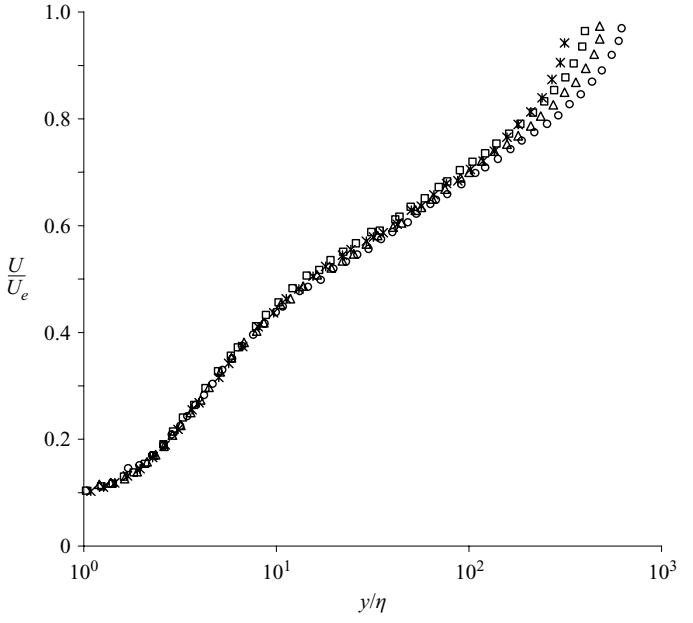

FIGURE 33. Mean velocity as a function of wall distance scaled with the external velocity U_e and the Kolmogorov length scale η. $Re_\theta = 8200$ (*); $Re_\theta = 11\,500$ (□); $Re_\theta = 14\,500$ (△); $Re_\theta = 20\,800$ (○).

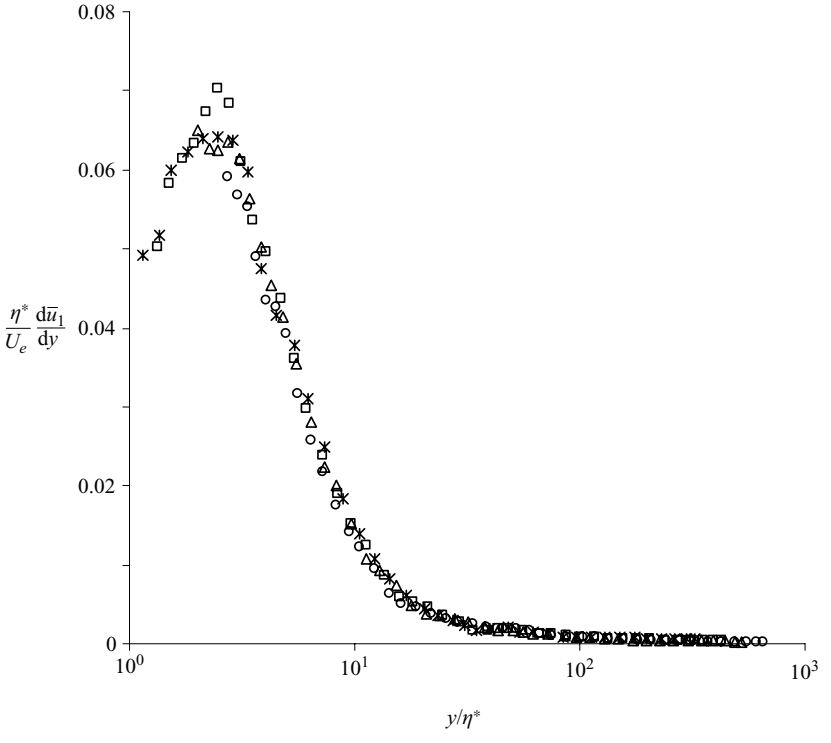

FIGURE 34. Mean velocity gradient as a function of wall distance scaled with the external velocity U_e and the clipped Kolmogorov length scale $\eta*$. $Re_\theta = 8200$ (*); $Re_\theta = 11\,500$ (□); $Re_\theta = 14\,500$ (△); $Re_\theta = 20\,800$ (○).

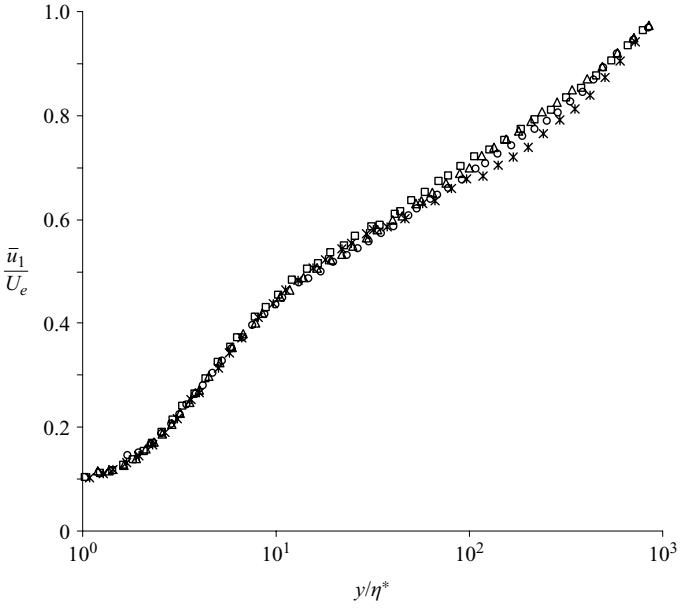

FIGURE 35. Mean velocity as a function of wall distance scaled with the external velocity U_e and the clipped Kolmogorov length scale η^*. $Re_\theta = 8200$ (*); $Re_\theta = 11\,500$ (□); $Re_\theta = 14\,500$ (△); $Re_\theta = 20\,800$ (○).

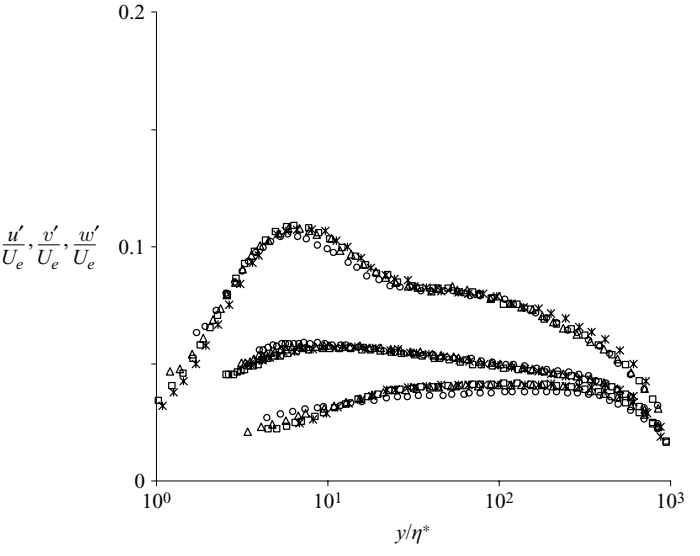

FIGURE 36. Turbulence intensities as a function of wall distance scaled with the external velocity U_e and the clipped Kolmogorov length scale $\eta*$. $Re_\theta = 8200$ (*); $Re_\theta = 11\,500$ (□); $Re_\theta = 14\,500$ (△); $Re_\theta = 20\,800$ (○).

so good for the Reynolds shear stress $\overline{u'v'}$. Here also, the lowest Reynolds number shows a slightly different shape, probably for the same reasons as mentioned above. Of more concern is the level problem at $Re_\theta = 20\,800$. The global shape and peak position are correct, but the overall level is too low. This discrepancy is attributed here

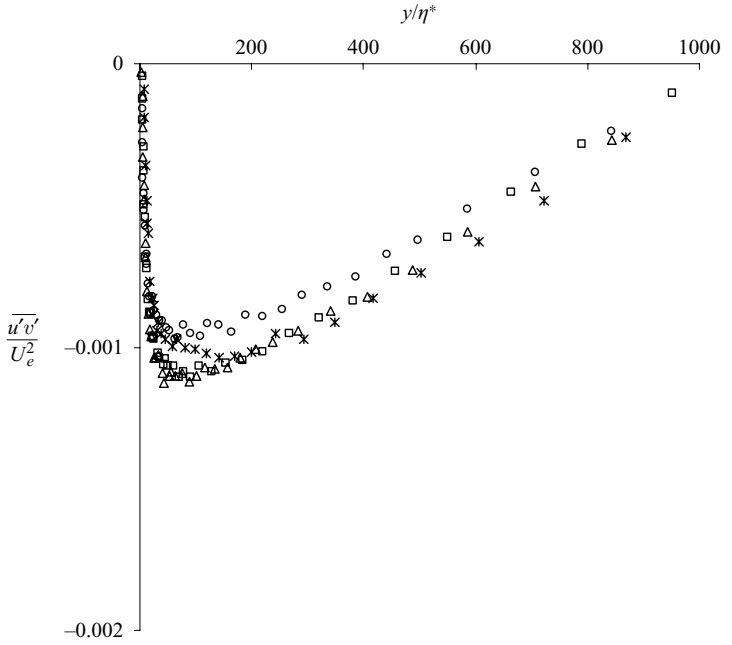

FIGURE 37. Reynolds shear stress as a function of wall distance scaled with the external velocity U_e and the clipped Kolmogorov length scale $\eta*$. $Re_\theta = 8200$ (*); $Re_\theta = 11\,500$ (□); $Re_\theta = 14\,500$ (△); $Re_\theta = 20\,800$ (○).

to measurement errors: this quantity is very difficult to measure with hot wires and even in wall units (see Carlier & Stanislas 2005, figure 8), the universality is not good. These errors were recently highlighted by Lin (2006) using PIV in planes parallel to the wall. Consequently, it can be said that, in the present range of confidence, figures 34 to 37 support the above analysis and the proposed scaling.

It is, of course, of interest at this stage to see at which wall distance y^* the scale η^* switches from η to $\delta/1000$. This result is given in figure 38 as y^*/δ as a function of Re_θ . It can be seen that this parameter increases linearly with Reynolds number. For comparison, the thickness of the log layer (estimated from the velocity profiles) is also given in figure 38 as δ_{log}/δ. It is clear from this figure that, as the Reynolds number increases, a growing part of the wake region scales on U_e and η. This supports the idea that the dynamic range of scales in the boundary layer has to be large enough (about three orders of magnitude) for the Kolmogorov scales to be representative of the dissipation process only. It is to be noticed that this dynamic range is based on δ and not on y for the integral scales. This means that the largest integral scales present in the flow have to be taken into account and not the local ones. The value $y*/\delta = 1$ is of course of interest, as it corresponds to the limit at which the whole boundary layer would scale with η. Using the fit given in figure 38, this value is obtained for $Re_\theta \approx 35\,000$. This result supports the idea that at high enough Reynolds number, in strong analogy with the laminar case, the turbulent boundary layer could become universal when scaled with the single set of parameters U_e and η. For that to be true, the Kolmogorov length scale η has simply to be smaller than $\delta/1000$ in the whole boundary-layer thickness. Such a Reynolds number is not so high and can be reached already in some existing experimental facilities. Of course, the situation is not as simple here as in laminar flows. The Kolmogorov scale η, contrary to ν, is not

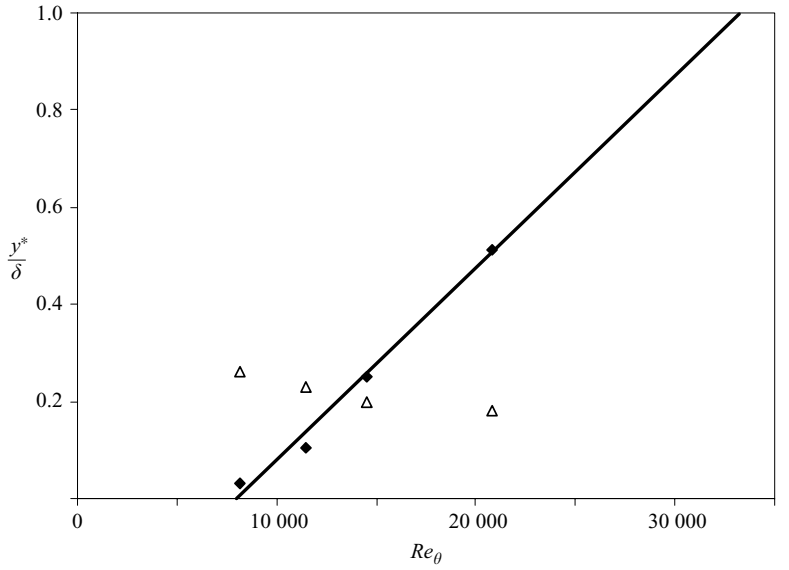

FIGURE 38. Ordinate $y*$ of Kolmogorov length scale clipping as a function of Reynolds number Re_θ . $y*/\delta$ (◆); best least-squares fit (—); δ_{log}/δ (△).

a property of the fluid but of the turbulence and it is seen to vary with y (figure 6) and also with x. Nevertheless, this result seems to contradict the ongoing idea that at high Reynolds number, the boundary layer-becomes dominated by the large scale outer structures. It seems from the present analysis that all the information required from the outer flow is contained in U_e and that it is the Kolmogorov length scale which fixes all the rest, by characterizing the way the kinetic energy of the mean flow is dissipated.

As a last point in this discussion, it is worth rearranging (7.1), taking into account that $\eta\upsilon/\nu = 1$. This leads us to express the wall friction as:

$$\frac{\tau_w}{\frac{1}{2}\rho\upsilon^2} \simeq 8. \tag{7.3}$$

This equation can be compared to the one given by a standard similarity analysis taking ρ, U_e, and any length scale as primary variables:

$$\frac{\tau_w}{\frac{1}{2}\rho U_e^2} = f(Re).$$

The comparison of these two equations leads to the conclusion that some internal similarity should exists when using the Kolmogorov scales in the very near-wall region ($y^+ < 30$). This opens the way for some interesting theoretical investigations.

8. Conclusion

An analysis of velocity fields acquired with highly-resolved stereoscopic PIV in the logarithmic region of a turbulent boundary layer has been conducted in a plane normal both to the mean flow and the wall, at Reynolds numbers $Re_\theta = 7800$ and 15 000. A two-point spatial correlation tensor of the signed swirling strength, linear stochastic estimation and a vortex identification algorithm have been used to characterize more or less streamwise oriented eddies and their interaction. This analysis reveals that

the most probable structure is asymmetric, corresponding to a one-legged hairpin vortex (while the mean structure, as evidenced for example by Hutchins *et al.* (2005) is symmetric). It also appears that for vortices, the boundary-layer can be roughly divided into two main regions: a near-wall region, lower than $y^+ \approx 150$, densely populated by eddies that interact with each other through different mechanisms of generation and destruction; and a logarithmic region where vortex interactions happen less frequently and where vortices are mainly submitted to stretching by the mean and fluctuating shear stresses. In this logarithmic region, Reynolds number and wall-normal independences of the probability density functions of the vortex radius and intensity are obtained when these quantities are scaled by the Kolmogorov length and time scales, respectively. This result corroborates those obtained by Kang *et al.* (2005) in their DNS of a channel flow. The p.d.f.s and most probable values of radius and maximum azimuthal velocity obtained here are in good agreement with the findings of these authors. As proper scaling is obtained over the entire range of detected scales in both the present study and in the numerical investigation of Kang *et al.* (2005), it suggests that the vortex dynamics is the same in the whole range of Reynolds number. A detailed analysis of the transport equation for the mean square of the fluctuating vorticity indicates that, in the log and buffer layer (but not in the viscous sublayer), these dynamics are mainly driven by the balance between viscous dissipation on one side and vortex stretching by mean and turbulent strain rates on the other.

Based on these observations, the structure of the inner layer can be revisited and described in terms of layers of increasing order of magnitude with respect to the Kolmogorov scale ($\approx 1,\ \approx 10, \approx 100, \approx 1000$). This leads us to propose a new formulation of the wall friction and to propose a new scaling of the near-wall region flow based on U_e and η. This scaling works in the range of Reynolds number under study and can be smoothly linked to the standard external scaling by defining a length scale η^* using (7.2). The mean velocity profile and the main components of the Reynolds stress tensor show good universality when scaled with U_e and η^*. The region scaling with η grows linearly and rapidly with Reynolds number. This opens a perspective of universal scaling of the whole boundary layer with these two parameters for Re_θ larger than 30 000 to 40 000. This is the range of interest for most practical applications, including aeronautics.

The authors would like to thank Dr M. Tanahashi for providing the data of the vortex characteristics used in figures 17 and 24 from the DNS performed in his group (Kang *et al.* 2005). Most of the analysis of the enstrophy equation and the discussion were done during a sabbatical stay of M. S. at the LTRAC Laboratory of Monash University in Melbourne (Australia). He would like to warmly thank Pr Julio Soria for the nice atmosphere and the discussions which have surely contributed to the progress of the work. The PIV data processed here were recorded in a joint experiment with Dr C. Kaehler (Tu Braunschweig), who is acknowledged.

Part of this work was performed under the WALLTURB European project. WALLTURB (a European synergy for the assessment of wall turbulence) is funded by the CEC under the 6th framework program (Contract N: AST4-CT-2005-516008).

REFERENCES

Adrian, R. J. 1991 Particle-imaging techniques for experimental fluid mechanics. *Annu. Rev. Fluid Mech.* **23**, 261–304.

Adrian, R. J. 1993 Stochastic estimation of conditional structure. *Eddy Structure Identification in Free Turbulent Shear Flows*. (ed. J. P. Bonnet & M. N. Glauser). Kluwer.

Adrian, R. J. 2007 Hairpin vortex organization in wall turbulence. *Phys. Fluids* **19**, 041301.

Adrian, R. J. & Moin, P. 1988 Stochastic estimation of organized turbulent structure: homogeneous shear flow. *J. Fluid Mech.* **190**, 531–559.

Adrian, R. J., Christensen, K. T. & Liu, Z. C. 2000*a* Analysis and interpretation of turbulent velocity fields. *Exps. Fluids* **29**, 275–290.

Adrian, R. J., Meinhart, C. D. & Tomkins, C. D. 2000*b* Vortex organization in the outer region of the turbulent boundary layer. *J. Fluid Mech.* **422**, 1–54.

Del Álamo, J. C. & Jimenez, J. 2006 Linear energy amplification in turbulent channels. *J. Fluid Mech.* **559**, 205–213.

Del Álamo, J. C., Jimenez, J., Zandonade, P. & Moser, R. D. 2004 Scaling of energy spectra of turbulent channels. *J. Fluid Mech.* **500**, 135–144.

Del Álamo, J. C., Jimenez, J., Zandonade, P. & Moser, R. D. 2006 Self similar vortex clusters in the turbulent logarithmic region. *J. Fluid Mech.* **561**, 329–356.

Brooke, J. W. & Hanratty, T. J. 1993 Origin of turbulence producing eddies in a channel flow. *Phys. Fluids* **5**, 1011–1022.

Carlier, J. 2001 Étude des structures cohérentes de la turbulence de paroi à grand nombre de Reynolds par Vélocimétrie par image de particules. PhD thesis, Université des Sciences et Technologies de Lille, France.

Carlier, J. & Stanislas, M. 2005 Experimental study of eddy structures in a turbulent boundary layer using particle image velocimetry. *J. Fluid Mech.* **535**, 143–188.

Chakraborty, P., Balachandar, S. & Adrian, R. J. 2005 On the relationships between local vortex identification schemes. *J. Fluid Mech.* **535**, 189–214.

Choi, W. C. & Guezennec, Y. G. 1989 On the asymmetry of structures in turbulent boundary layers. *Phys. Fluids* **2**, 628–630.

Chong, M. S., Perry, A. & Cantwell, B. J. 1990 A general classification of three-dimensional flow fields. *Phys. Fluids* A**2**, 765–777.

Christensen, K. T. & Adrian, R. J. 2001 Statistical evidence of hairpin vortex packets in wall turbulence. *J. Fluid Mech.* **431**, 433–443.

Das, S. K., Tanahashi, M., Shoji, K. & Miyauchi, T. 2006 Statistical properties of coherent fine eddies in wall-bounded turbulent flows by direct numerical simulation. *Theor. Comput. Fluid Dyn.* **20**, 55–71.

Foucaut, J., Carlier, J. & Stanislas, M. 2004 PIV optimization for the study of turbulent flow using spectral analysis. *Meas. Sci. Technol.* **15-6**, 1046–1058.

Foucaut, J., Stanislas, M. & Kostas, J. 2006 Wall shear stress measurement using stereoscopic PIV. *12th Int Symp. on Flow Vizualization, September 10–14, 2006, Gottingen, Germany*.

Ganapathisubramani, B., Longmire, E. K. & Marusic, I. 2003 Characteristics of vortex packets in turbulent boundary layers. *J. Fluid Mech.* **478**, 35–46.

Ganapathisubramani, B., Hutchins, N., Hambleton, W. T., Longmire, E. K. & Marusic, I. 2005 Investigation of large-scale coherent structures in a turbulent boundary layer using two-point correlations. *J. Fluid Mech.* **524**, 57–80.

Ganapathisubramani, B., Longmire, E. K. & Marusic, I. 2006 Experimental investigation of vortex properties in a turbulent boundary layer. *Phys Fluids* **18**, 055105.

Graaf, D. B. D. & Eaton, J. K. 2000 Reynolds number scaling of the flat plate turbulent boundary layer. *J. Fluid Mech.* **422**, 319–346.

Guezennec, Y. 1989 Stochastic estimation of coherent structures in turbulent boundary layers. *Phys Fluids* A **1**, 1054–1060.

Guezennec, Y., Piomelli, U. & Kim, J. 1989 On the shape and dynamics of wall structure in turbulent channel flow. *Phys Fluids* A **1**, 764–766.

Hambleton, W., Hutchins, N. & Marusic, I. 2006 Simultaneous orthogonal-plane particle image velocimetry measurements in a turbulent boundary layer. *J. Fluid Mech.* **560**, 53–64.

Hanratty, T. J. & Papavassiliou, D. V. 1997 The role of wall vortices in producing turbulence. In *Self–Sustaining Mechanisms of Wall Turbulence* (ed. R. L. Panton). Computational Mechanics Publications.

Head, M. R. & Bandyopadhyay, P. 1981 New aspects of turbulent boundary layer structure. *J. Fluid Mech.* **107**, 297–338.

Hoyas, S. & Jimenez, J. 2006 Scaling of the velocity fluctuations in turbulent channels up to $Re_\tau = 2003$. *Phys. Fluids* **18**, 011702.

Hutchins, N., Hambleton, W. T. & Marusic, I. 2005 Inclined cross-stream stereo particle image velocimetry mearsurements in turbulent boundary layers. *J. Fluid Mech.* **541**, 21–54.

Jimenez, J. & Wray, A. A. 1998 On the characteristics of vortex filaments in isotropic turbulence. *J. Fluid Mech.* **373**, 255–285.

Jimenez, J., del-álamo, J. C. & Flores, O. 2004 The large scale dynamics of near wall turbulence. *J. Fluid Mech.* **505**, 179–199.

Kähler, C., Stanislas, M., Dewhirst, T. P. & Carlier, J. 2000 Investigation of the spatio-temporal flow structure in the log-law region of a turbulent boundary layer by means of multi-plane stereo particle image velocimetry. Selected paper presented at the *10th Intl Symp. on Applications of Laser Technology to Fluid Mechanics, Lisbon (Portugal)* Springer.

Kang, S. J., Tanahashi, M. & Miyauchi, T. 2005 Dynamics of fine scale eddy clusters in turbulent channel flows. In *Fourth Intl Symp. on Turbulence and Shear Flow Phenomena, Williamsburg, VA, USA*, pp. 183–188.

Klewicki, J. 1989 Velocity vorticity correlation related to the gradients of the reynolds stresses in parallel turbulent wall flows. *Phys. Fluids* A **1**, 1285–1288.

Lin, J. 2006 Detailed study of the coherent structures of the buffer layer of wall turbulence using stereo particle image velocimetry. PhD thesis, l'Ecole Centrale de Lille (in English).

Panton, R. L. 1997 *Self–Sustaining Mechanisms of Wall Turbulence*. Computational Mechanics Publications.

Perry, A. E. & Chong, M. S. 1982 On the mechanism of wall turbulence. *J. Fluid Mech.* **119**, 173–217.

Perry, A. E. & Marusic, I. 1995 A wall-wake model for the turbulence structure of boundary layers. Part 1. Extension of the attached eddy hypothesis. *J. Fluid Mech.* **298**, 389–407.

Pope, S. B. 2000 *Turbulent Flows*. Cambridge University Press.

Priyadarshane, P., Klewicki, J., Treat, S. & Foss, J. 2007 Statistical structure of the turbulent boundary layer velocity-vorticity products at high and low Reynolds number. *J. Fluid Mech.* **570**, 307–346.

Robinson, S. K. 1991 Coherent motions in the turbulent boundary layer. *Annu. Rev. Fluid Mech.* **23**, 601–639.

Spalart, P. R. 1989 Theoretical and numerical study of the three-dimensional turbulent boundary layer. *J. Fluid Mech.* **205**, 319–340.

Stanislas, M., Foucaut, J.-M., Laval, J.-P. & Jie, L. 2005 Experimental study of coherent structures in a turbulent boundary layer using PIV. In *Fourth Intl Symp on Turbulence and Shear Flow Phenomena, Williamsburg, VA, USA*, pp. 45–50.

Tanahashi, M., Miyauchi, T. & Ikeda, J. 1997 Scaling law of coherent fine structure in homogeneous isotropic turbulence. In *11th Symp. Turbulence and Shear Flow*, pp. 4-17–4-22.

Tanahashi, M., Iwase, S. & Miyauchi, T. 2001 Appearance and alignment with strain rate of coherent fine eddies in turbulent mixing layer. *J. Turbulence* **2**.

Tanahashi, M., Kang, S. J., Miyamoto, T., Shiokawa, S. & Miyauchi, T. 2004 Scaling law of fine scale eddies in turbulent channel flows up to $Re_\tau = 800$. *Intl J. Heat Fluid Flow* **25**, 331–340.

Tennekes, H. & Lumley, J. L. 1972 *A First Course in Turbulence*. MIT Press.

Theodorsen, T. 1952 Mechanism of turbulence. In *Proc. 2nd Midwest. Conf. Fluid Mech., 2nd edn*, Ohio State University, Columbus, Ohio, pp. 1–18.

Tomkins, C. D. & Adrian, R. J. 2003 Spanwise structure and scale growth in turbulent boundary layers. *J. Fluid Mech.* **490**, 37–74.

Wu, Y. & Christensen, K. 2006 Population trends of spanwise vortices in wall turbulence. *J. Fluid Mech.* **568**, 55–76.

Zhou, J., Adrian, R. J., Balachandar, S. & Kendall, T. M. 1999 Mechanisms for generating coherent packets of hairpin vortices in channel flow. *J. Fluid Mech.* **387**, 353–396.